# A Technique for High-Speed Microscopic Imaging of Dynamic Failure Events and Its Application to Shear Band Initiation in Polycarbonate

Providence, RI 02912 e-mail: pinkesh\_malhotra@alumni.brown.edu

Brown University, 184 Hope Street,

P. Malhotra<sup>1</sup>
School of Engineering,

S. Niu
School of Engineering,
Brown University,
184 Hope Street,
Providence, RI 02912
e-mail: Sijun niu@brown.edu

# V. Srivastava

School of Engineering,
Brown University,
184 Hope Street,
Providence, RI 02912
e-mail: vikas\_srivastava@brown.edu

# P. R. Guduru

School of Engineering, Brown University, 184 Hope Street, Providence, RI 02912 e-mail: Pradeep\_Guduru@brown.edu An experimental technique is reported, which can image the deformation fields associated with dynamic failure events at high spatial and temporal resolutions simultaneously. The technique is demonstrated at a spatial resolution of ~1 µm and a temporal resolution of 250 ns, while maintaining a relatively large field of view ( $\approx 1.11 \text{ mm} \times 0.63 \text{ mm}$ ). As a demonstration, the technique is used to image the deformation field near a notch tip during initiation of a shear instability in polycarbonate. An ordered array of 10 µm diameter speckles with 20 µm pitch, and deposited on the specimen surface near the notch tip helps track evolution of the deformation field. Experimental results show that the width of the shear band (SB) in polycarbonate is approximately 75 µm near the notch tip within resolution limits of the experiments. The measurements also reveal formation of two incipient localization bands near the crack tip, one of which subsequently becomes the dominant band while the other is suppressed. Computational simulation of the experiment was conducted using a thermomechanically coupled rate-dependent constitutive model of polycarbonate to gain further insight into the experimental observations enabled by the combination of high spatial and temporal resolutions. The simulation results show reasonable agreement with the experimentally observed kinematic field and features near the notch tip, while also pointing to the need for further refinement of constitutive models that are calibrated at high strain rates ( $\sim 10^5/s$ ) and also account for damage evolution. [DOI: 10.1115/1.4053080]

Keywords: high-speed microscopy, particle tracking, shear bands, spatial resolution, temporal resolution, viscoplasticity, finite deformation, polycarbonate model, computational mechanics, constitutive modeling of materials, dynamics, flow and fracture, impact, mechanical properties of materials, plasticity, thermodynamics, wave propagation

#### 1 Introduction

In situ imaging of dynamic events has been of interest in experimental mechanics for a long time. High-speed imaging has been used in a wide range of disciplines to study a variety of events such as cavitation [1], combustion [2–5], shock waves [6–8], adiabatic shear localization [9–14], crack tip deformation fields [15–17], twinning [18], and dynamic friction [6-8]. The advancements in imaging of such dynamic events have been enabled by the rapid evolution of high-speed camera technologies over the past 70 years and the high temporal resolution that they offer. At the same time, there are several dynamic phenomena that occur not only at small time-scales but also at small length-scales, examples of which include hot-spot mechanisms in energetic materials; dynamic failure of heterogeneous materials through crack propagation [19,20], adiabatic shear bands (SBs), twinning, dynamic friction, and cavitation. Imaging such events requires high temporal and spatial resolutions simultaneously, i.e., high-speed microscopy. The importance of high-speed microscopy in advancing our understanding of dynamic response and failure of materials has been highlighted in a recent National Research Council report [21].

Significant progress has been reported in the recent literature on imaging at high spatial and temporal resolutions simultaneously. Rubino et al. [8] reported an investigation on laboratory earthquakes in which rupture of frictional interfaces was investigated by combining high-speed imaging with the digital image correlation (DIC) technique. The combination allowed them to measure the deformation and stress fields associated with shear shock waves and evolution of dynamic friction coefficient at the interface. Based on the imaging technology and magnification reported in their work, the spatial resolution of imaging can be inferred to be 27.8  $\mu$ m based on the Nyquist criterion (sensor pixel pitch p =30  $\mu$ m, magnification = 2.16). Kannan et al. [18] reported a study on dynamic twinning in single crystal magnesium by using highspeed photography. They used a 105 mm Nikon lens coupled with two teleconverter lenses and bellows in order to spatially resolve twin nucleation and propagation. Based on the numbers reported in their paper, imaging was done at a magnification of  $5 \,\mu \text{m}$  per pixel, which implies a pixel-limited spatial resolution of  $10 \,\mu\text{m}$ . Imaging at a temporal resolution of 200 ns, they measured twin tip velocities of the order of 1 km/s; twin boundary growth values and twin tip velocities of second-generation twins that nucleate from boundaries of pre-existing twins were also reported. Estrada et al. [1] used micro-cavitation as a rheometer to measure viscoelastic properties of polyacrylamide gel under high strain

<sup>&</sup>lt;sup>1</sup>Corresponding author.

Contributed by the Applied Mechanics Division of ASME for publication in the JOURNAL OF APPLIED MECHANICS. Manuscript received October 3, 2021; final manuscript received November 18, 2021; published online December 8, 2021. Assoc. Editor: Hareesh Tippur.

rates. A pulsed laser was used to generate cavitation which was imaged using a Phantom v2511 high-speed camera and bright-field illumination with a halogen lamp. Images of bubble generation, collapse, and subsequent oscillations were taken at a spatial resolution of  $5.52~\mu m$  and a temporal resolution of  $3.7~\mu s$ . Combining bubble kinematics with a constitutive model allowed them to extract material properties of the gel in a minimally invasive manner. Ravindran et al. imaged polymer-bonded sugar (PBS) [22,23] subjected to high strain rate loading to identify deformation localization mechanisms. They used Photron SAX2 high-speed camera at 100,000 fps along with a Navitar extension tube and appear to have achieved a pixel-limited spatial resolution of  $20~\mu m$ . Using DIC to analyze the deformation field, they showed that large strain localization occurs in polymer rich areas between crystal boundaries while the deformation of crystals is minimal.

It is clear that there is a great deal of interest in measuring kinematic fields at high spatial and temporal resolutions simultaneously in order to understand the deformation response and failure mechanisms in heterogeneous materials. Here, we present a technique that offers such a capability with a temporal resolution of 250 ns, spatial resolution of about  $1\,\mu m$ , and a field of view of about  $1.1\,mm \times 0.63\,mm$ . Section 2 presents the experimental setup.

## 2 Experimental Setup

A schematic of the experimental setup is shown in Fig. 1. The key components of the high-speed microscopy system are (a) a

high-speed camera, (b) imaging optics, and (c) illumination. The considerations that determined the choices made in assembling the experimental setup are described first.

**2.1 High-Speed Camera.** Dynamic deformation and failure events in solids typically occur over times scales of a few microseconds, which necessitates a high-speed camera with framing rates of  $10^6 \, \mathrm{s^{-1}}$  or higher. As explained below, they also require a sufficiently large sensor (i.e., pixel array size of  $1000 \times 1000$  or greater) and a fine pixel pitch to image at an acceptable field of view combined with micron-scale spatial resolution. In addition, low electronic noise of the camera is a requirement for measuring the kinematic fields through DIC or particle tracking, particularly for large deformations. Among the three most used technologies for the present-day high-speed cameras are (a) single complementary metal-oxide semiconductor (CMOS) sensor cameras, (b) gated-intensified cameras, and (c) rotating mirror cameras.

The single-sensor in situ storage cameras are the most popular high-speed cameras at present. These cameras use a CMOS sensor and on-chip storage of all frames, which allows them to run at high frame rates. Depending on the read-out mechanism, these sensors can offer varying resolutions at different frame rates. Typically, the sensor resolution decreases as the frame rates go up. This is due to limitations placed on the read-out speeds, i.e., the speed at which an acquired image can be transferred to the memory. However, certain cameras offer constant resolution at all frame rates. Among the best specifications for these

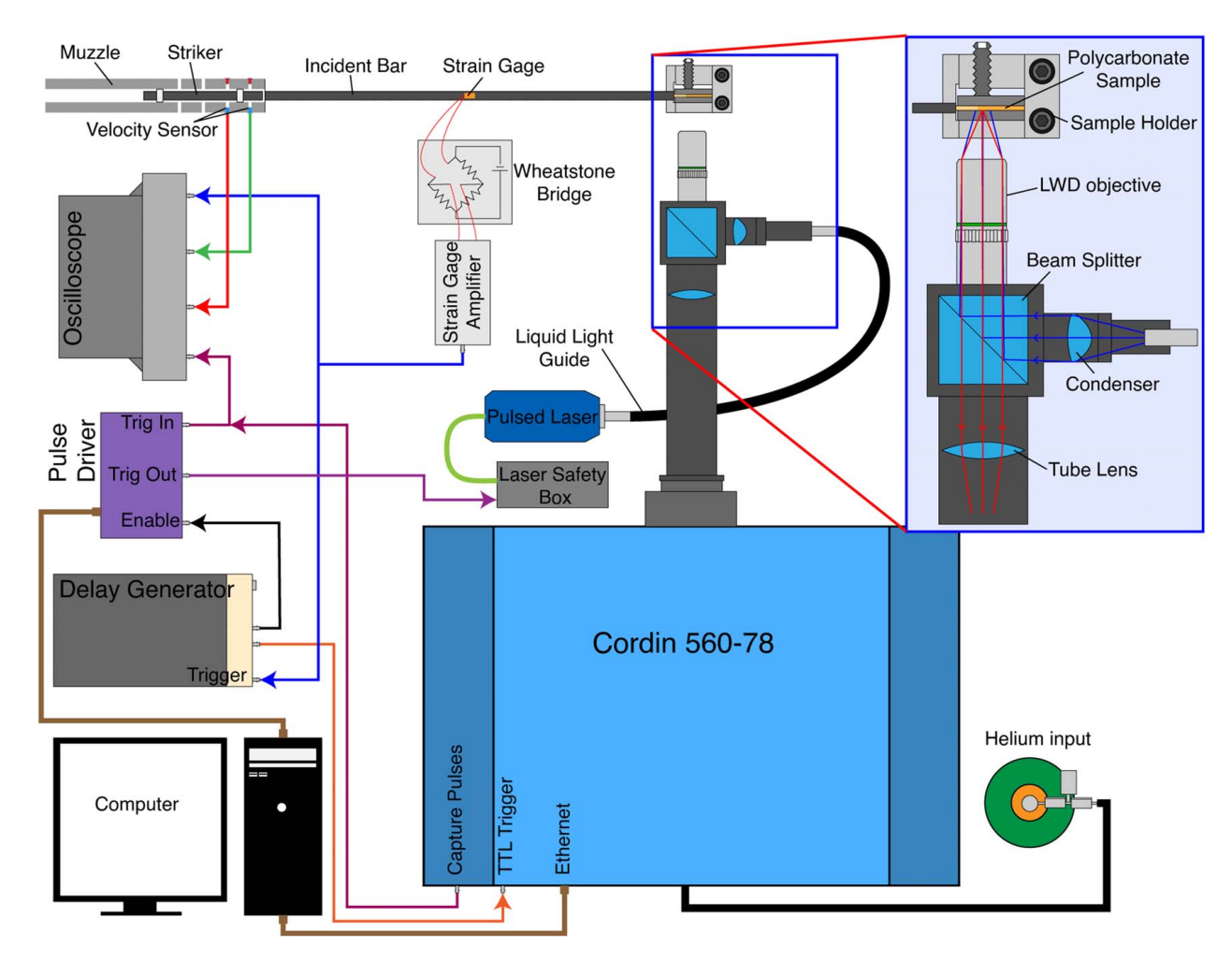


Fig. 1 A schematic of high-speed microscope setup for imaging a sample impacted in a Kolsky bar. Key components of the system are high-speed camera, microscope optics, and the laser for illumination. Cable connections between various components are shown using arrows. The inset on the right shows the optical elements in detail. Illuminating rays are shown in blue and image forming rays in red. (Color version online.)

commercial cameras are (a) sensor size of  $400 \times 250$  pixels<sup>2</sup>, (b) image acquisition rate of 5 million frames per second, and (c) the number of frames collected is 128. These cameras tend to be lighter and more compact compared with the rotating mirror and gated-intensified cameras but usually have large pixel size ( $\sim 30 \ \mu m$ ) and lower sensor resolution. The sensor chip architecture also leads to lower fill factors ( $\sim 37\%$ ) which can cause aliasing and inability to resolve higher spatial frequency content.

The gated intensifier cameras consist of an image intensifier unit, coupling optics, and a CCD sensor. The heart of these cameras is the image intensifier unit which can amplify the incoming photons by a factor of over 1000. The intensification is achieved through a microchannel plate (MCP) that amplifies the photoelectrons received from the photocathode and sends them to a phosphor screen for conversion back to photons. The intensifier comes with an added advantage of electronic gating which allows extremely small exposure durations, of the order of nanoseconds. These cameras can offer framing rates of up to a few hundred million fps with 200 ps exposures and collect up to eight frames. However, they suffer from larger noise, loss of contrast, and poorer spatial resolution [24,25], which are inherent to the intensification process and optical coupling in this design. As mentioned in Ref. [8], extracting useful quantitative information like displacements and strains from images taken using an intensified CCD camera is not easy, especially to meet the stringent requirements of displacement, velocity, and strain resolutions. Also, the total number of frames is small, which may not be sufficient for capturing the full evolution of dynamic events.

Rotating mirror cameras consist of multiple independent CCD sensors spaced equally in two 120 deg arcs, positioned radially with respect to a rotating mirror at the center. A light beam hitting the mirror is swept across each of the arcs and focused on the CCDs by relay lenses. A helium gas-turbine is used to drive the mirror at high speeds, which yields framing rates of up to a few million fps. The advantage of the rotating mirror cameras is that the individual CCD sensors can be configured to have a large pixel array with a small pitch to increase the spatial resolution (to be discussed below). On the other hand, these cameras are bulky and heavy; and their operation is much more complex compared with the other technologies.

High-speed microscopy requires integration of a high-speed camera and an optical microscope. The achievable temporal resolution of such a system is determined by the framing rate of the high-speed camera. All the high-speed imaging technologies described above satisfy the time-resolution requirements for imaging many dynamic events in solids; however, they differ in the spatial resolution that can be practically achieved. The spatial resolution of any optical imaging system is limited either by the numerical aperture of the objective lens (diffraction limit) or the pixel size of the imaging detector (sampling limit). The diffraction limit, given through the Rayleigh criterion, can be expressed as

$$r_{obj,d} = \frac{\lambda}{2 NA} \tag{1}$$

where  $\lambda$  is the wavelength of the illuminating light and NA is the numerical aperture of the objective. On the other hand, pixel-limited spatial resolution of an imaging system can be defined using the Nyquist criterion as

$$r_{obj,p} = \frac{2p}{m} \tag{2}$$

where  $r_{obj,p}$  is the finest feature that can be resolved, p is the pixel pitch, and m is the magnification of the optical imaging system. The spatial resolution of the system is given by the larger of  $r_{obi,p}$  and  $r_{obi,d}$ . There is a wide range of commercially available microscope objectives, which reduces the task of satisfying the Rayleigh criterion to one of the proper optical design and integrating the microscopy optics with those of the high-speed camera. However, the characteristics of the imaging sensors in commercially available high-speed imaging cameras often set limits on the imaging resolution, minimum required magnification, and the field of view. Table 1 illustrates the trade-offs for six different commercial highspeed cameras. The table presents the minimum required magnification of the optics and the achievable field of view for a target spatial resolution of  $0.5 \,\mu\text{m}$ . Note that in the case of gated intensifier cameras, the resolution of the MCP can set the resolution limit instead of the sensor pixel pitch. From Table 1, it can be seen that the minimum optical magnification required for achieving the target spatial resolution and the corresponding field of view at that resolution differ widely between the cameras considered. An optical system with a higher magnification has a correspondingly lower depth of field, which limits the allowable out of plane motion of the specimen during an experiment while keeping it in focus. Moreover, a higher magnification objective tends to have a smaller working distance, requiring it to be very close to the dynamically deforming specimen surface (it could be as close as a millimeter at high magnifications), which could be impractical. Thus, the combination of lowest required magnification and the largest field of view provides a practical criterion of choosing an appropriate high-speed camera.

Based on these considerations (cf., Table 1), a rotating mirror camera has been chosen in this investigation despite the complexity of its technology, operation, and maintenance. The Cordin 560 rotating mirror high-speed camera used in the present setup consists of 78 independent CCD sensors; the mirror can rotate at a speed of up to 16,667 rotations per second, which gives a maximum framing rate of 4 million fps. Each CCD is a monochrome 14-bit sensor with a  $1920 \times 1080$  pixel array and a pixel pitch of  $7.4 \, \mu \text{m}$ . The camera body has approximate dimensions of  $24 \, \text{in} \times 30 \, \text{in} \times 26 \, \text{in}$ . and weighs about  $100 \, \text{kg}$ . However, since it operates as a microscope, it is necessary to be able to move it at micron-scale precision for alignment and focusing purposes. A 6-degree of freedom stage has been custom-designed and built to meet these requirements with the camera mounted on it (Fig. 2).

In addition to the above considerations, since one is often interested in imaging dynamic events, there are additional constraints on the illumination system to minimize motion blur and the need

Table 1 A comparison of six commercially available high-speed cameras with respect to their ability to capture images at a spatial resolution of  $0.5 \, \mu m$ 

	Technology	Maximum framing rate (fps)	Number of frames	Sensor pixel array size	Pixel pitch (µm)	MCP resolution	Magnification, $m \text{ for } r_{obj} = 0.5 \ \mu\text{m}$	Field of view (mm <sup>2</sup> )
1	Rotating mirror	4 million	78	$1920 \times 1080$	7.4	_	44×	$0.48 \times 0.27$
2	Single CMOS sensor	5 million	180	$924 \times 768$	30	_	120×	$0.23 \times 0.19$
3	Single CMOS sensor	5 million	128	$400 \times 250$	30	_	120×	$0.1 \times 0.06$
4	Image intensifier	200 million	8	$2000 \times 2000$	7.4	40 lp/mm or 25 $\mu$ m	100×	$0.15 \times 0.15$
5	Image intensifier	333 million	16	$1360 \times 1024$	6.45	50 lp/mm or $20 \mu m$	80×	$0.11 \times 0.08$
6	Image intensifier	200 million	8	$1360 \times 1024$	6.7	28 μm	112×	$0.08 \times 0.06$

Note: The parameters of interest are the minimum magnification required to achieve this spatial resolution and the corresponding field of view. The illumination wavelength is assumed to be 640 nm

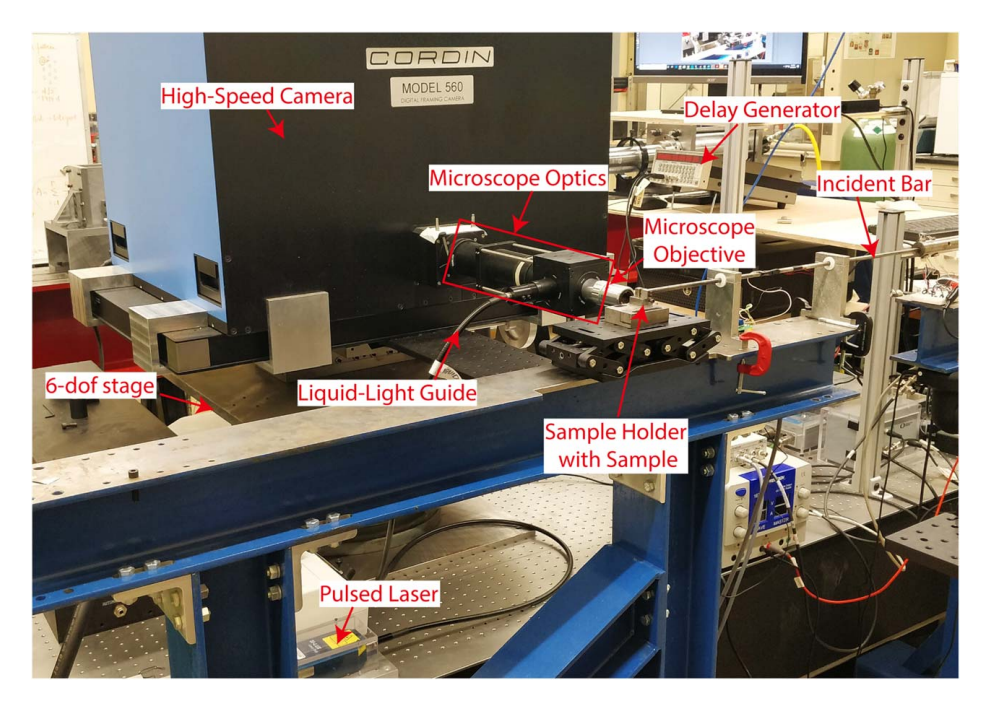


Fig. 2 High-speed microscope setup at Brown University. The important components of the system are highlighted: Cordin high-speed camera mounted on a 6-dof stage, microscope optics, microscope objective, pulsed laser, the liquid light guide that carries illumination pulses from the pulsed laser to the condenser lens for in-line illumination and the delay generator that acts the master clock to synchronize all events. The incident bar and sample holder with the sample are also shown.

to make use of the available dynamic range of the imaging sensors. Further details are discussed in Sec. 2.3.

2.2 Optics. The optical imaging system consists of a microscope that forms an image of the specimen surface on a prescribed plane at the entrance of the camera, from where it is relayed by the internal optics to the sensor plane via the rotating mirror. The microscope elements are shown in Fig. 2. The main elements are an infinity-corrected long working distance objective and a tube lens. An in-line illumination arrangement is chosen, where the illumination light enters the optical train normal to the optical axis and is directed into the objective through a 50:50 beam splitter as shown. A liquid light guide feeds light from a laser illumination source to an aspheric condenser lens, the relative position of which with respect to the end of the light guide determines the illumination spot size on the specimen. A Koehler-type illumination can be achieved by adjusting the condenser lens position to form the image of the end of the light guide on the back focal plane of the objective. On the other extreme, a highly focused spot can be achieved by adjusting the condenser lens such that it collimates the light from the liquid light guide. In our experiments, an intermediate configuration is chosen such that the illumination spot size on the specimen surface is slightly larger than the field of view. Diffuse reflection from the specimen is collected by the objective (see inset

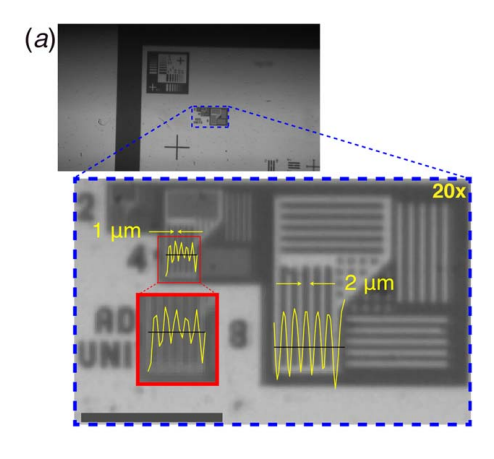
in Fig. 1) and a tube lens forms a real image on the prescribed plane near the entrance to the camera. A Nikon F-mount connects the microscope optics to the camera. The system is configured for three long working distance microscope objectives: 10x, 20x, and 50x. Table 2 shows the details of the objectives, the combined magnification of the microscope optics and the camera internal optics. spatial resolution, the limiting criterion that determines the spatial resolution (diffraction limited versus sampling limited), and the field of view. Figure 3 demonstrates that the calculated spatial resolutions are indeed realized; it shows images of a resolution target with the 20x and the 50x objectives. The former can resolve 1  $\mu$ m features and the latter can resolve 0.5  $\mu$ m features. Microscope optics and illumination (described in Sec. 2.3) have been customdesigned to serve the purpose of attaining large spatiotemporal resolutions simultaneously. The know-how has been shared with Cordin, which has made it commercially available.

**2.3 Illumination.** The combination of high temporal and spatial resolutions places severe requirements on the illumination. Since the interest is in imaging dynamic events, image blur due to object motion must be minimized. As an example, consider the case of the characteristic particle velocity within the field of view to be of the order of 100 m/s. To restrict the particle displacement during optical exposure (i.e., motion blur) to be within the

Table 2 A comparison of different objectives used in the optical train of the high-speed microscope setup

Objective	NA	Working distance	$m_{total}$	Spatial resolution	Limiting criterion	Field of view
10×Plan Apo Infinity-Corrected Long Working Distance Objective 20×Plan Apo Infinity-Corrected Long Working Distance Objective 50×Plan Apo Infinity-Corrected Long Working Distance Objective	0.42	34 mm 20 mm 13 mm	6.67× 13.33× 33.33×	2.22 μm 1.11 μm 0.58 μm	Pixel-Limited Pixel-Limited Diffraction limited	2.13×1.20 mm <sup>2</sup> 1.07×0.60 mm <sup>2</sup> 0.43×0.24 mm <sup>2</sup>

Note: All objectives are long working distance objectives. As the magnification increases, the working distance decreases and the spatial resolution increases. The  $50 \times$  objective gives the highest resolution of  $0.58 \ \mu m \ m_{total} = m_{objective} \times 2/3$ .



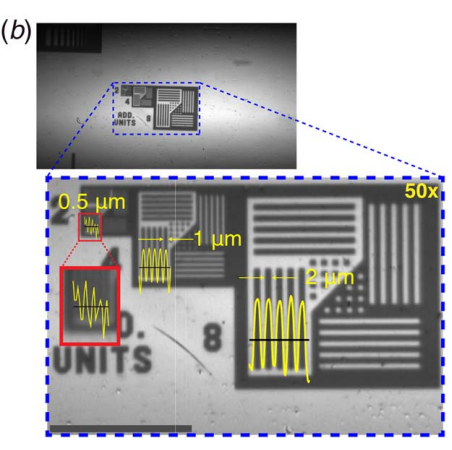


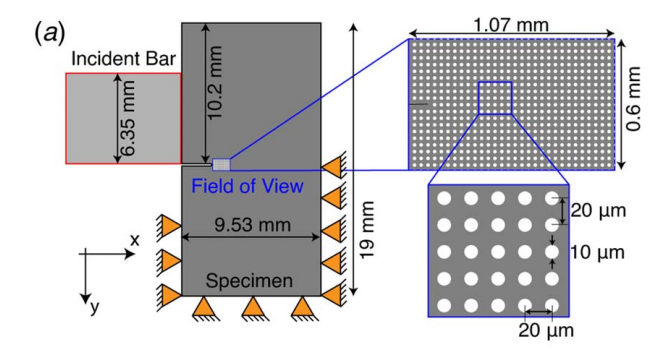
Fig. 3 Demonstration of imaging resolution using a resolution target with groups of  $2\,\mu\text{m}$ ,  $1\,\mu\text{m}$ , and  $0.5\,\mu\text{m}$  wide lines. The images are taken using a (a) 20x and (b) 50x objective. For each magnification, a full-resolution image is shown on the left while the region of interest is outlined in a dashed blue line and a magnified view shown right below the full image. The yellow curves are variations in intensity across a group of lines. As shown in Table 2, the 20x objective has a calculated resolution of  $1\,\mu\text{m}$ , which is demonstrated by its ability to resolve the  $1\,\mu\text{m}$  and  $2\,\mu\text{m}$  wide lines. The 50x objective system has a calculated resolution of  $0.58\,\mu\text{m}$ , which is demonstrated by its ability to resolve the  $0.5\,\mu\text{m}$  wide lines. Note that the images have been cropped to show the area of interest and do not represent the entire field of view. The length of the scale bar is  $50\,\mu\text{m}$  in both images. (Color version online.)

imaging resolution (say 1  $\mu$ m), the illumination duration must be no more than 10 ns for each frame. A pulsed laser is a convenient source for generating a sequence of such short illumination pulses. Another vital difference between high-speed imaging with a large field of view of the order of a centimeter and highspeed microscopy is that in the latter each pixel of the CCD sensor collects photons from a very small area of the specimen surface. In the system under consideration here, for a magnification of 20x, each pixel collects photons from an area of approximately  $0.56 \,\mu\text{m} \times 0.56 \,\mu\text{m}$ . In order to make use of the dynamic range of the CCD pixels and obtain sufficient image contrast, the number of photons collected by each pixel multiplied by its quantum efficiency needs to be a significant fraction of the CCD full well depth, which in the present case is 44,000 electrons. Based on this number, one can calculate the power requirement on the laser source by accounting for the losses along the optical path (for example, losses in the light guide, passing through the beam splitter twice, diffuse reflectivity of the specimen surface, collection efficiency of the objective, etc.) and the finite illumination pulse width. Such a calculation, based on a pulse width of 10 ns, shows the required power to be a few hundred Watts. To satisfy the requirement, a Specialized Imaging LUX640 pulsed laser source is used to illuminate the specimen, which is a 400 W pulsed laser that emits a low coherence beam at a wavelength of  $640 \pm 10$  nm (cf., Fig. 1).

## 3 Experimental Demonstration

The capability of the experimental system is demonstrated by imaging the initiation of a SB from a notch tip in a polycarbonate specimen subjected to impact loading in a Kolsky bar. SBs are zones of intense plastic shear strain that are typically formed under high strain rates as a result of a competition between material hardening and softening mechanisms. SBs have been extensively studied in a variety of materials including metals, alloys, bulk metallic glasses, and polymers [9,26]. However, in the context of real time imaging, it is worth mentioning a few relevant references that report measurement of strain and stress fields in the vicinity of initiating and propagating SBs [11,13,27-29]. These efforts used a typical field of view of a few centimeters and measured the far field stress and strain fields that correspond to the mixed mode loading of the pre-existing notch. A phenomenological criterion for SB initiation could be formulated in terms of the mixed mode loading parameters (for example, the stress intensity factors) and their rates. For example, in the context of edge-impact of notched plate experiments [12,27-29], it was reported that a locally mode-I crack initiated for impact velocities below a critical value and a SB initiated above it. At the same time, as reported in Refs. [13,30], a postexperiment microscopic investigation of the specimens that failed in mode-I showed the presence of an initiated and arrested SB at the notch tip. Interestingly, the local mode-I crack that propagated at an oblique angle initiated from the notch tip-not from the arrested SB tip. In other words, even at velocities below the critical velocity for mode transition, a SB initiated at the notch tip, propagated, and got arrested, before reflected waves from the specimen boundary modify the notch tip stress field to force the crack to initiate in a different mode. As such, a high-speed microscopy capability offers the benefit of capturing the sequence of events at the micron-scale more accurately. For the purposes of this study, the well-studied edge-notched plate configuration is used, which was impact loaded in a Kolsky bar. Polycarbonate is chosen as the specimen material, partly motivated by a prior investigation of similar nature by Ravi-Chandar [29].

Specimens were cut from a Lexan 9034 polycarbonate sheet and have the following dimensions:  $19 \text{ mm} \times 9.53 \text{ mm} \times 1.5 \text{ mm}$ (Fig. 4(a)). A pre-crack is made in the polycarbonate sample at the tip of the machined notch using a sharp razor. The specimen is constrained in a steel fixture to enforce the boundary conditions shown in Fig. 4(a). An edge-on impact is carried out on the specimen using the incident bar of the Kolsky bar. The incident bar is 6.3 mm in diameter, 61 cm in length and is made of C350 maraging steel. A striker of the same diameter and material and a length of 15.24 cm sends a compressive pulse of 50  $\mu$ s duration through the incident bar. Imaging is done with a 20x objective. The deformation field is measured through particle tracking by depositing a grid of 10  $\mu$ m diameter circular copper dots with a pitch of 20  $\mu$ m in both directions (Fig. 4). The dots were deposited near the crack tip using a lift-off photolithography process, as illustrated in Fig. 1 in Supplemental Section 1 available in the Supplemental Materials on the ASME Digital Collection. The polycarbonate sample is cleaned with isopropanol using sonication. The sample is spincoated with LOR-5A photoresist followed by a hard-bake at 100 ° C in an oven. Another photoresist, AZ1505A, is spin-coated on top of the previous layer and soft-baked at 95 °C. A maskless aligner (MLA150, Heidelberg Instruments) was used to selectively expose the photoresists at a calibrated exposure intensity of 150 mJ/cm<sup>2</sup>. The photoresist is developed using CD-26 (nine parts CD-26 and one part DI water) for 60 s, followed by a DI water rinse. An O<sub>2</sub> plasma de-scumming process is performed before the metal deposition process. A 200 nm layer of Cu is deposited using an e-beam evaporator (Kurt J. Lesker). Final lift-off is done with



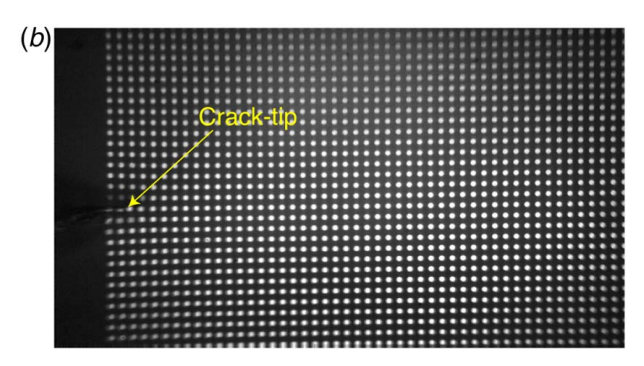


Fig. 4 (a) Edge-on impact on the polycarbonate specimen. The specimen is fixed on the bottom half at the back to prevent rigid translation. Fixing on the bottom face and bottom half of the front face impedes rigid rotation. Lateral confinement (not shown here) is provided on either side of the specimen plate to minimize out of plane motion. The field of view with a 20x objective is shown. 10  $\mu \rm m$  sized Cu dots spaced 20  $\mu \rm m$  apart are used for particle tracking. (b) High-speed camera image of the specimen before the arrival of longitudinal compressive wave at the crack tip.

methanol in a sonicator. The copper dots form a reflective foreground against the transparent polycarbonate background, providing good contrast.

Experimental preparation consists of aligning the impact face of the specimen with the middle of incident bar cross section, followed by focusing the camera on the area of interest on the specimen surface. Strain gage signal from the incident bar is used to trigger the camera. An important element of the experimental procedure is to ensure that the illumination pulses are synchronized with the optimal mirror positions with respect to the CCD sensors by accounting for signal delays at many interfaces in the experimental setup. The corresponding signal timing diagram is shown in Fig. 5.

As alluded to earlier, depth of field is an important consideration in any microscopy application, particularly in high-speed microscopy where out-of-plane movement of the specimen surface is unavoidable due to the deformation itself. The effective depth of field for the present application is characterized experimentally by translating the specimen along the optical axis and imaging the specimen (see Fig. 6). An out-of-plane displacement of 25  $\mu m$  does not result in a significant loss in the definition of dots. However, at a displacement of 62.5  $\mu m$ , some of the neighboring dots begin to coalesce with each other, but individual dots can still be distinguished, which can thus be treated as the "practical" depth of field for the purposes of imaging the dot pattern.

# 4 Results and Discussion

Figure 7 shows a sequence of images of the dot pattern when the striker impact speed is 17.4 m/s. The images were acquired at a rate of 4 million frames/s, but the sequence presents only a selected set

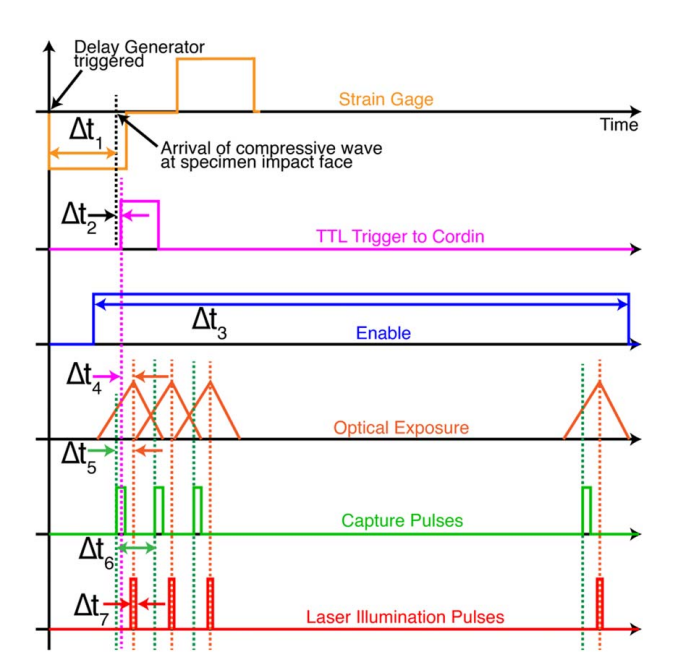


Fig. 5 A typical timing diagram at a frame rate of 4 million fps. Assume that the incident wave arrives at the strain gage at t=0and at this instant, the strain gage triggers the Delay Generator. At  $t = \Delta t_1$  (  $\approx$ 60  $\mu$ s), the compressive incident wave arrives at the specimen impact face. A 5 V transistor-transistor logic (TTL) trigger is then sent to the camera at  $t = \Delta t_1 + \Delta t_2$  where  $\Delta t_2$ accounts for the time delay between impact at specimen interface and the time when compressive wave first reaches the notch tip. An Enable signal with a pulse width of  $\Delta t_3$  is sent to the Laser Pulse Driver (a unit that controls synchronization of laser illumination pulses with input pulses from the camera) before the camera is triggered. There is a time gap of  $\Delta t_4$ between the TTL trigger to the camera and the alignment of the rotating mirror with the first charge-coupled device (CCD) after the trigger signal is received. Due to the mirror rotation, optical exposure of each CCD is not uniform during one inter-frame time period, which is depicted using triangular pulses. The optimal location of exposure lies at the peak of these pulses, whereby the rotating mirror is said to be aligned to the CCD. Illumination pulses need to be centered at these peaks. This is achieved by sending capture pulses from the camera to the Laser Pulse Driver in advance by a time duration of  $\Delta t_5$ .  $\Delta t_5 =$ 0.185  $\mu$ s is found to work well.  $\Delta t_6$  indicates the inter-frame time (=250 ns at 4 million fps). An illumination pulse width,  $\Delta t_7 = 20$  ns, is used in these experiments but this width can be brought down to 5 ns.

of images, showing the evolution of deformation upon arrival of the loading wave and subsequent initiation of a SB at the notch tip. A video of the event generated by collating the individual images is included in the supplemental material on the ASME Digital Collection. Even without quantitative analysis, one can visualize the strain field evolution from the change in the slope of the lines connecting the dots along vertical and diagonal directions in the undeformed configuration. The notch tip plastic zone is evident through the appearance of a dark region and degraded focus due to the out of plane motion of the specimen surface. However, it is still possible to identify the positions of the dots through image processing as illustrated in Fig. 7(f).

The first step in extracting the displacement and strain field from the images is to correct for slight differences in the fields of view of successive images. As noted above, the Cordin camera consists of 78 different CCD sensors. Since light is relayed through a different optical path for the formation of each image, slight differences in the extent and orientation between successive images are expected. For more details, see Kirugulige et al. [31]. Since the particle tracking algorithm used here is sensitive to such misalignments, it is necessary to correct the images to set the same global coordinate axes

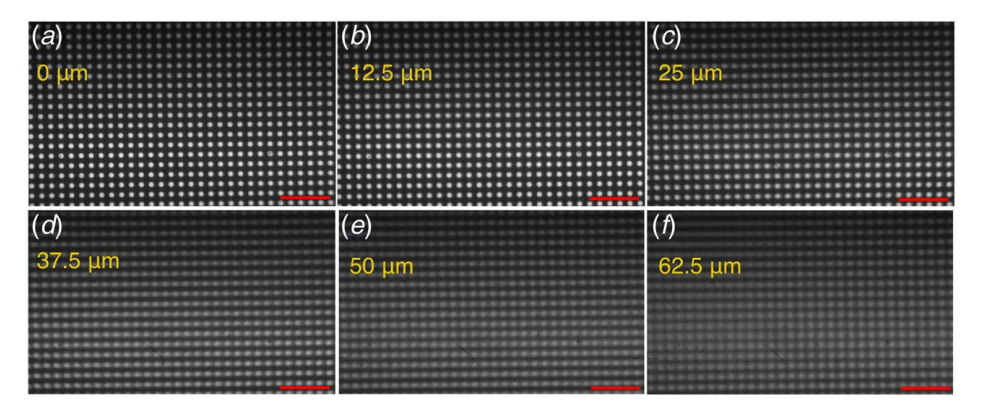


Fig. 6 "Practical" depth of field measurements for the optics with the  $20\times$  objective using a grid pattern of circular dots. The dots are  $10\,\mu{\rm m}$  in diameter and spaced  $20\,\mu{\rm m}$  apart. A sample with these dots is mounted on a translation stage and moved toward the objective, starting from the focused position in (a). In (b)-(f), the sample is moved in increments of  $12.5\,\mu{\rm mm}$  to a final position of  $62.5\,\mu{\rm mm}$  away from the focused position. At this point, the image becomes blurry, and the neighboring dots begin to coalesce with each other. Note that the entire field of view is not shown. A scale bar of  $100\,\mu{\rm m}$  length is shown in red at the bottom corner of each image.

on all images. The procedure followed here is similar to that used by Kirugulige et al. [31]. A camera calibration is performed by imaging a static sample with a grid pattern of 50  $\mu$ m circular dots, spaced 100  $\mu$ m apart (see Fig. 8(a)). All images are thresholded and binarized, followed by locating the centroids of the dots. One of the 78 CCD images is chosen as a reference and centroid locations in the rest of the frames are tracked with respect to the reference

image. It is assumed that the optical distortion of the images can be modeled as a homogeneous deformation. Therefore, the coordinates in these images can be related to the coordinates in the reference image through a transformation of the form

$$\begin{pmatrix} x_i \\ y_i \end{pmatrix} = \begin{bmatrix} a & b \\ c & d \end{bmatrix} \begin{pmatrix} x_0 \\ y_0 \end{pmatrix} + \begin{pmatrix} e \\ f \end{pmatrix}$$
 (3)

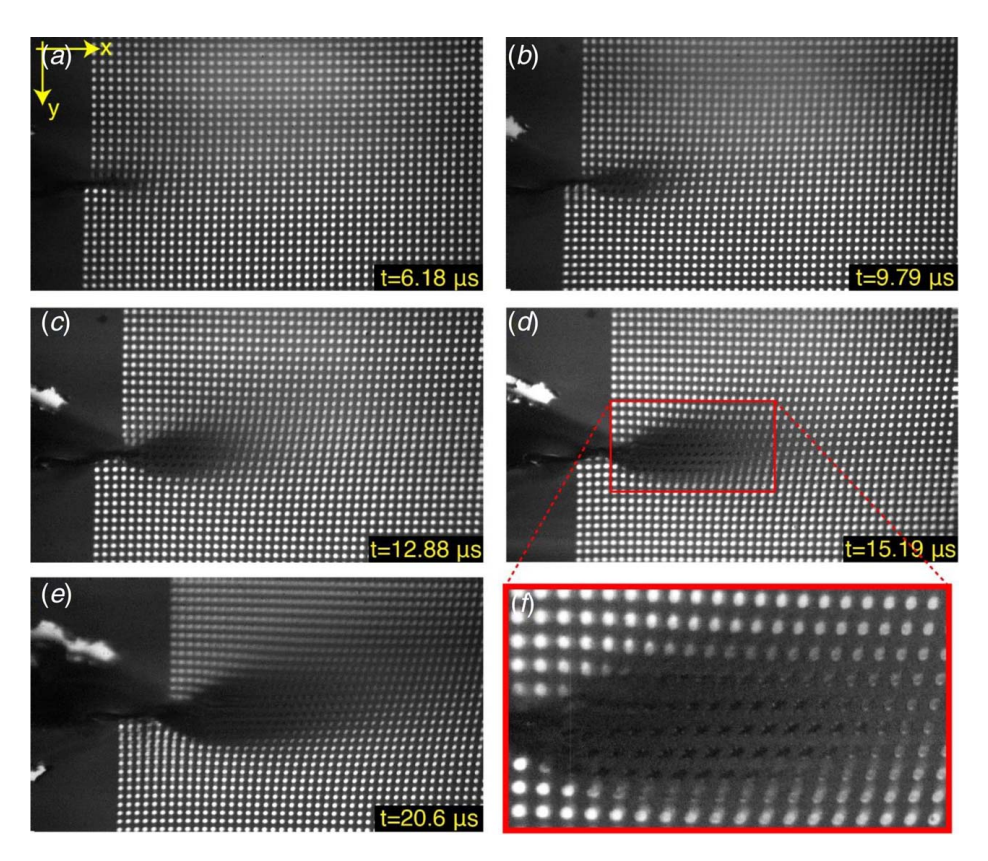


Fig. 7 As acquired images of the notched polycarbonate plate undergoing deformation taken at different time instants: (a)  $t=6.18~\mu s$ , (b)  $t=9.79~\mu s$ , (c)  $t=12.88~\mu s$ , (d)  $t=15.19~\mu s$ , and (e)  $t=20.6~\mu s$ . The images were taken at a frame rate of 3,883,495 fps. As the deformation progresses, a zone of localized plastic deformation forms ahead of the crack tip. Particle tracking is performed until  $t=15.19~\mu s$ . By  $t=20.6~\mu s$ , the top half of the specimen has moved ahead of the lower half by  $\approx 120~\mu m$ , indicating the development of a large shear strain. Deformation in the vicinity of the notch tip at  $t=15.19~\mu s$  is shown in a magnified view in (f).

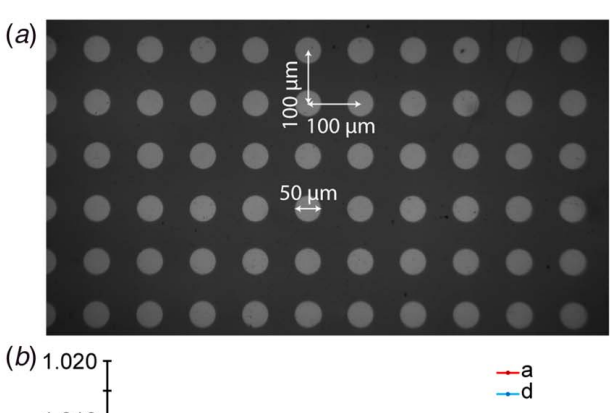
where  $(x_i, y_i)$  are coordinates of deformed images,  $(x_0, y_0)$  are coordinates of the reference image, the matrix with (a, b, c, d) constants corresponds to the assumed homogeneous deformation gradient, and the vector (e, f) corresponds to in-plane rigid translation. The unknown constants are determined using least-squares minimization. A set of these unknowns is shown in Figs. 8(b)-8(d). The diagonal components (a, d) of the deformation gradient differ from 1 by less than 1% and the off-diagonal components (b, c), which represent the shearing/rotation, are less than 0.5% for the most part. However, the rigid translations e and f are significant. Hence, a set of static images is obtained just prior to each dynamic experiment, which is used to determine the correction constants for each experiment. All experimental parameters such as the frame rate, illumination settings, and delays are kept identical between the static imaging and the actual dynamic experiment that follows immediately. The correction constants are used to perform an inverse transform to align each image with the reference image.

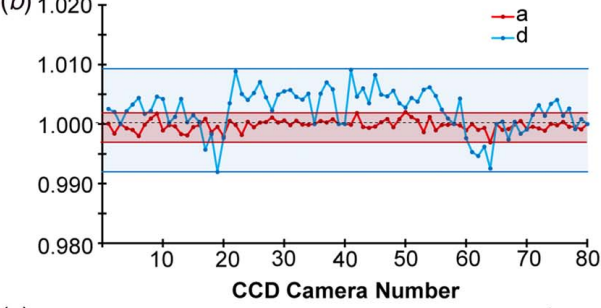
**4.1 Particle Tracking.** Particle tracking has been used in this study to calculate the displacement field. Another commonly used method for measuring deformation fields is DIC. Individual particles are tracked in particle tracking to infer displacements directly, whereas in DIC, the displacements at a given point are obtained after establishing correlation of a subset of pixels. To achieve similar resolution with DIC, speckles with sizes significantly smaller than the current particle size are needed. Since the current technique involves a relatively small depth of field and is sensitive to out of plane motions, smaller speckles would get blurred at smaller deformations, which is expected to result in a poorer correlation and hence larger errors, especially in the shear band region where deformation gradients are large. While particles in particle tracking also suffer from blurring, the effects are expected to be smaller due to larger particle sizes.

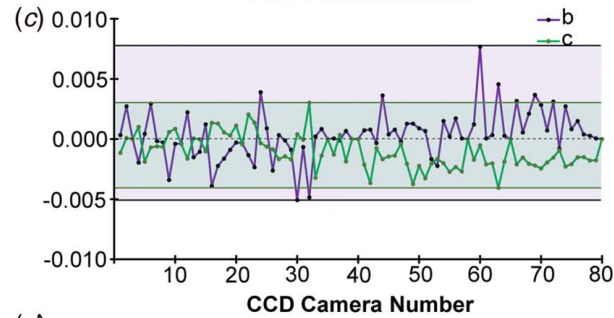
Particle tracking involves two steps: (a) identifying positions of particles in each image and (b) tracking the trajectories of individual particles across all frames to deduce displacements. The first step can be carried out with pixel-scale accuracy using Gaussian fitting [32–34] or radial symmetry methods [35,36]. Particles can then be tracked using nearest neighbor search, relaxation methods [37–39], feature vector based methods [40], and topology-based methods [41] among several others. In general, average interparticle distance is an important parameter in single particle tracking methods. It is not possible to resolve sinusoidal displacements with a period smaller than inter-particle distance according to the Nyquist criterion. Therefore, to resolve high spatial frequency content, smaller inter-particle distance and hence higher particle density are favorable. An inter-particle distance of 20  $\mu$ m is used here, which was found to be satisfactory.

For the first step of locating the particles, all images are thresholded and binarized to extract regions corresponding to each particle/dot. The centroid of each particle is chosen as the representative of its location. Due to intensity gradients across the image, a small subset of the particles could not be thresholded in a few images. A GUI is written in MATLAB 2019a (The MathWorks Inc., Natick, MA) to interactively allow for manual addition of approximate centroid locations for these particles, which are subsequently refined by Gaussian fitting to obtain more accurate centroid estimates. For the second step of tracking the particles, an iterative tracking scheme is adopted, i.e., the image  $I_{t+\Delta t}$  is correlated to image  $I_t$ . A reference particle is chosen in all images.  $I_{t+\Delta t}$  is translated and overlaid on top of  $I_t$  so that the location of reference particles in the two images matches exactly. Following this, a nearest neighbor algorithm is used to match particles. Since the displacement between consecutive frames is substantially less than the interparticle distance, this simple scheme works well.

**4.2 Deformation Fields.** Displacements of particle centroids are determined by tracking their locations. These displacements are interpolated using a cubic,  $\mathbb{C}^2$  continuous, triangulation-based







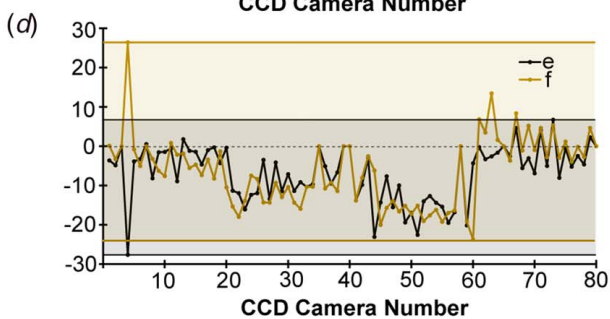


Fig. 8 (a) Grid pattern of circular dots used for CCD misalignment calibration. Constants for transformation matrix are shown in (b), (c), and (d). (d) Shows translations in pixel coordinates.

polynomial. Data points are obtained every 5 pixels  $(2.75 \, \mu \text{m})$  from the interpolated polynomial. To be able to reliably calculate gradients from the noisy displacement data, a nonlocal means (NLM) filter [42,43] is<sup>2</sup> used for de-noising and smoothing the displacement fields. The NLM filter preserves sharp displacement gradients expected in and around the shear band region. The usual "local" means filters smoothen a discrete field by taking the mean value of a group of neighboring values. This results in a lower noise level but at the cost of smoothing out sharp features. A "nonlocal" means filter, on the other hand, calculates a weighted mean of field values within a search window  $\Omega$  around the target location. The weights are chosen based on the similarity of  $N \times N$  neighborhoods within  $\Omega$ , to the  $N \times N$  neighborhood of the target location.

<sup>&</sup>lt;sup>2</sup>https://ch.mathworks.com/help/images/ref/imnlmfilt.html

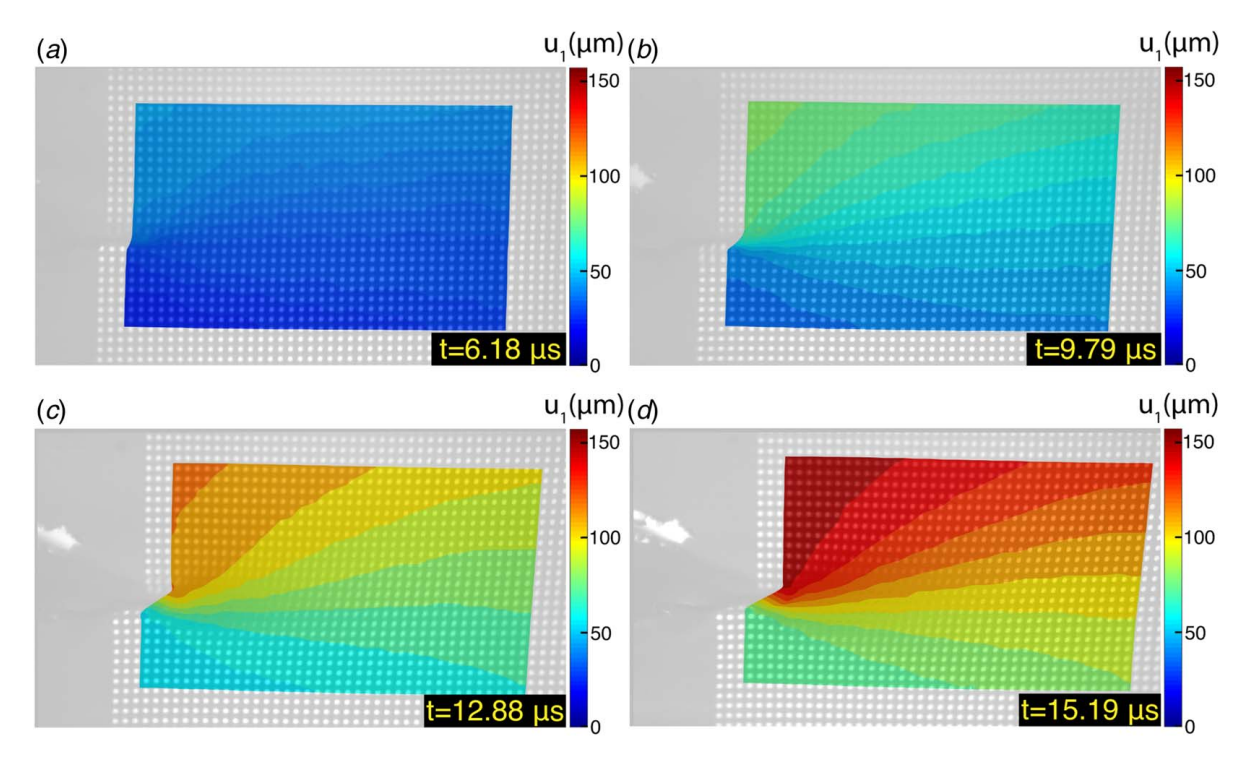


Fig. 9 Displacement in the x-direction,  $u_1$  plotted at (a)  $t = 6.18 \,\mu\text{s}$ , (b)  $t = 9.79 \,\mu\text{s}$ , (c)  $t = 12.88 \,\mu\text{s}$ , and (d)  $t = 15.19 \,\mu\text{s}$ . Contour values seen in the crack opening behind the notch tip is an artifact of displacement interpolation; no physical significance should be attributed to the same.

An exponentially decreasing function is typically used to assign weights, with the weight value decreasing with a decreasing degree of similarity. The degree of smoothing is controlled using a parameter  $h_s$  that controls the rate of decay of the weighting function. In this study, the NLM filter is applied to interpolated displacement fields. Here, we use a search window size  $\Omega = 7 \times 7$  data

points (= $81.6 \times 81.6 \,\mu\text{m}^2$ ), a neighborhood size N=7 data points (= $27.2 \,\mu\text{m}$ ) and a degree of smoothing  $h_s=0.5$ . The effect of NLM parameters on deformation fields is explored in the Supplemental Sections 2 and 3 available in the Supplemental Materials on the ASME Digital Collection. To reduce the temporal noise arising from uncertainty in centroid location for particles in the

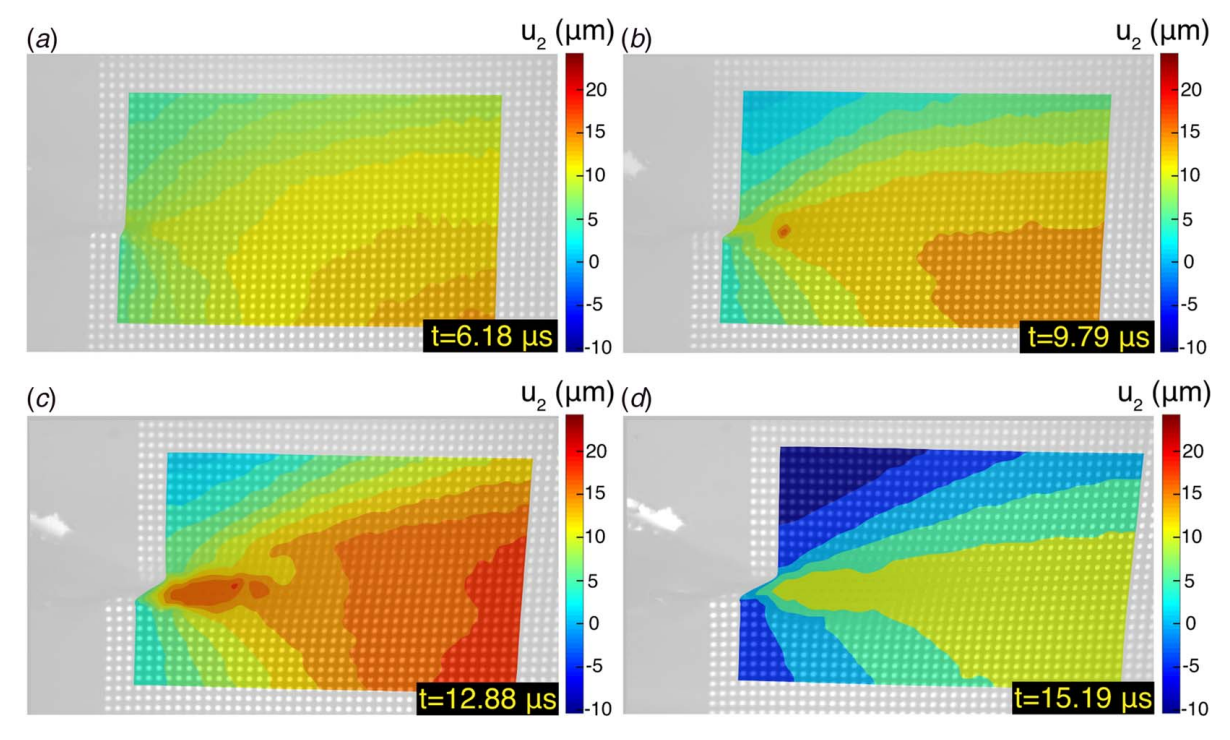


Fig. 10 Displacement in y-direction,  $u_2$  plotted at (a)  $t = 6.18 \,\mu\text{s}$ , (b)  $t = 9.79 \,\mu\text{s}$ , (c)  $t = 12.88 \,\mu\text{s}$ , and (d)  $t = 15.19 \,\mu\text{s}$ . Contour values seen in the crack opening behind the notch tip is an artifact of displacement interpolation; no physical significance should be attributed to the same.

vicinity of the highly deformed region at the notch tip (Fig. 7(f)), a mild temporal smoothing of displacement fields is performed using the "smooth" function in MATLAB. A degree of smoothing of 0.2 is used. Such a smoothing also helps reduce any CCD misalignment errors that remain after calibration.

The extracted  $u_1$  and  $u_2$  displacement fields are shown in Figs. 9 and 10, respectively, at four different instants of time. Note that all the deformation fields are evaluated from  $t = 1.55 \,\mu s$  to  $t = 15.19 \,\mu s$ . The compressive wave first reaches the left edge of the field of view at  $1.55 \,\mu s$ . It can be seen in Figs. 9 and 10 that there is a pronounced concentration of displacement contours at the crack tip which suggests large displacement gradients there, as expected. Note that  $u_1$  displacements are significantly larger than the  $u_2$  displacements, which is characteristic of the predominantly mode II loading of the notch tip. At the same time, the small specimen dimensions result in wave reflections from the boundaries, resulting in some crack opening displacement during the observation time window.

Strains are expressed in the form of a Green-Lagrange strain E, which is computed from the deformation gradient F as follows:

$$F = I + \nabla u \tag{4}$$

$$E = \frac{1}{2} [F^T F - I] \tag{5}$$

where u is the displacement field and I is identity tensor. Displacement gradients are found using a finite-difference scheme. At the boundaries, forward or backward finite-difference schemes are used. At the interior locations, central finite-difference scheme is used. The shear strain  $E_{12}$  is the most relevant quantity for studying shear localization; its evolution is plotted in Fig. 11. As the notch tip gets loaded by the stress waves from the impact face, a plastic zone develops at the notch tip. When the loading rate is sufficiently high, the plastic zone transitions into a SB. A complete characterization of SB initiation requires knowledge of the stress field as well, which

cannot be obtained directly from the kinematic fields being measured here. If the high strain rate constitutive response of the material is known, the stress field can be calculated from the measured strain field. At  $t = 6.18 \,\mu\text{s}$ , it can be seen that concentration of shear strain near the notch tip has already begun (Fig. 11(a)). The zone of plastic deformation evolves with time, leading to accumulation of shear strains as large as 1.4 in magnitude by  $t = 15.19 \,\mu\text{s}$ .

To gain further insight into evolution of shear strain and localization near the notch tip, it is instructive to examine the deformation of the dots along referential vertical lines (referred to as columns in the discussion below) at different distances from the notch tip, as illustrated in Figs. 12 and 13. Deformation of a column closer to the initial crack tip, i.e., column 5 and a column farther away from the crack tip, i.e., column 13 are plotted, to encompass the region of large shear strain. Figure 13 shows  $u_1$  and  $E_{12}$  as a function of position along the vertical coordinate (y) for these columns and their evolution with time. Each line corresponds to a different time, which is color coded as shown.

From Fig. 13(a), it can be clearly seen that as time evolves, the x-displacement of the fifth column of dots (c=5) is localized in an observable band of approximately 75  $\mu$ m in width, which is corroborated by the strain field shown in Fig. 13(c). However, the presence of a finer band below the resolution limit of the experimental measurement within the 75  $\mu$ m band cannot be ruled out. The strain field also shows that the localized zone of intense plastic shear strain increases in width with time before reaching a plateau. The width is found to increase as one moves away from the notch tip until a diffused plastic zone is reached at c = 13 (Figs. 13(b) and 13(d)). Figure 13(d) shows two local maxima in the shear strain along the y-direction at earlier times, indicating the formation of two bands. However, at later times ( $|t> \sim 10 \mu s|$ ), one of the bands takes over the localization process while the other gets suppressed. It is important to note that the accuracy of the strain values reported here is bound by the resolution limit imposed by the discreteness of the measurement points (i.e., the dots). Further improvements in the

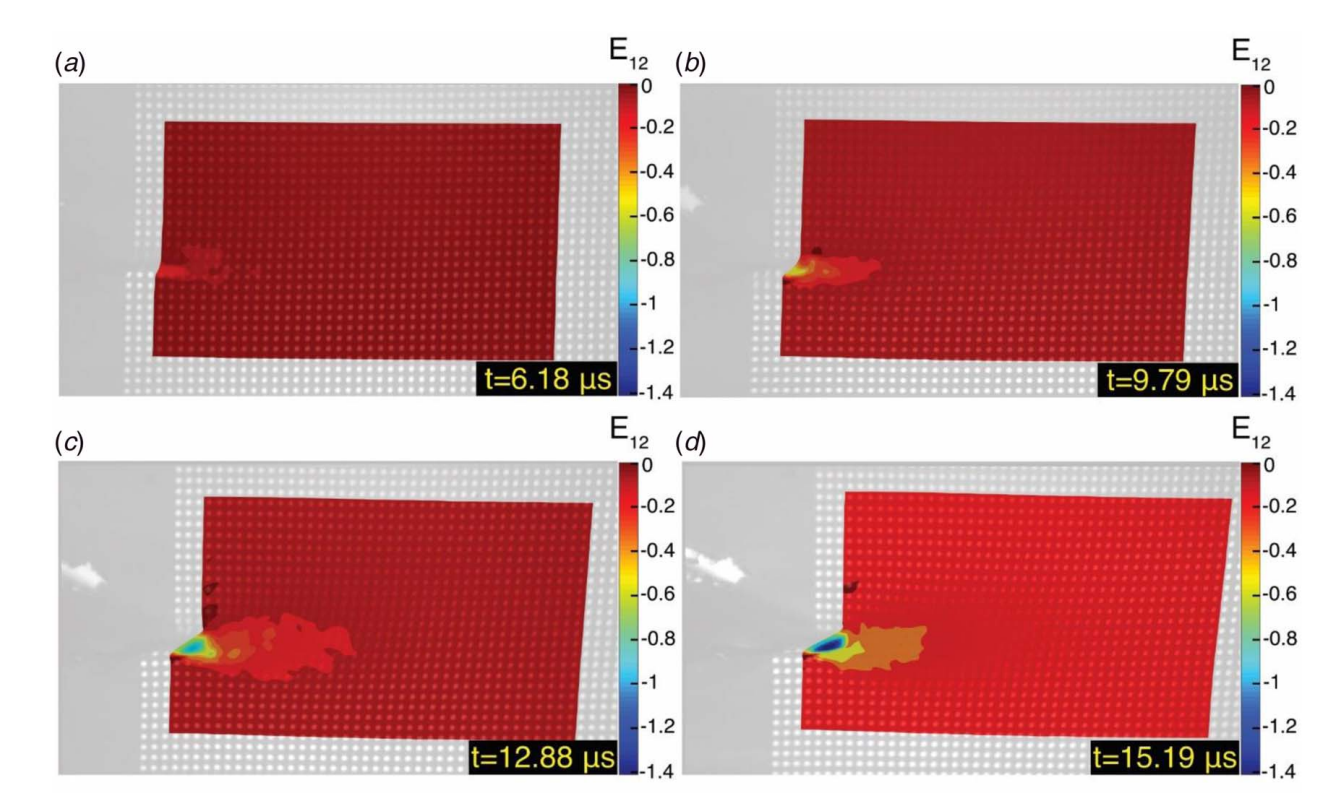


Fig. 11 Lagrangian shear strain,  $E_{12}$  plotted at (a)  $t = 6.18 \,\mu$ s, (b)  $t = 9.79 \,\mu$ s, (c)  $t = 12.88 \,\mu$ s, and (d)  $t = 15.19 \,\mu$ s. Contour values seen in the crack opening behind the notch tip is an artifact of displacement interpolation; no physical significance should be attributed to the same.

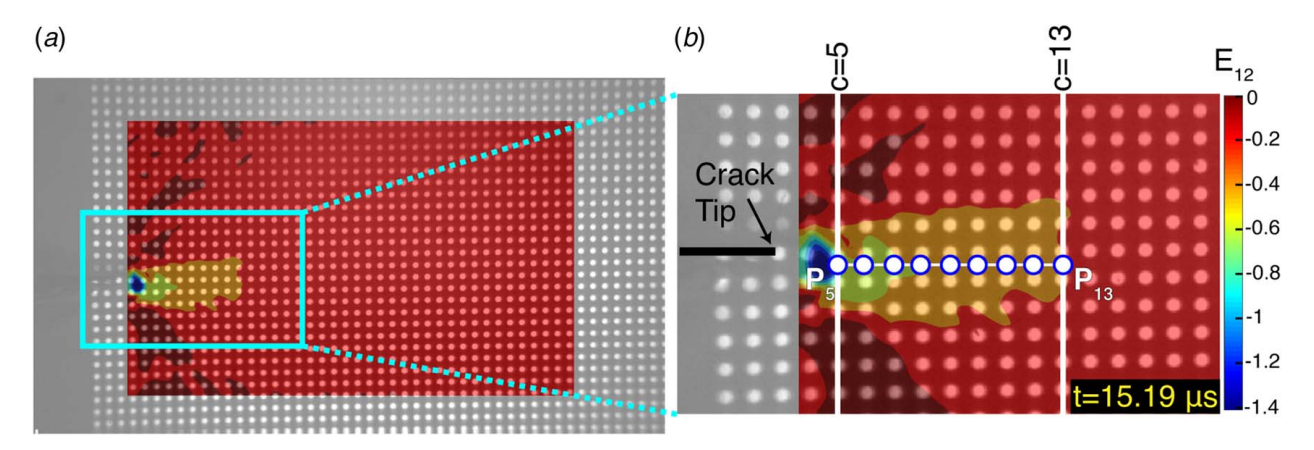


Fig. 12 (a) Shear strain,  $E_{12}$  field at  $t=15.19\,\mu s$  plotted on the reference undeformed image. (b) A zoomed in figure showing query locations for displacements, strains, and strain rates. Deformation along columns c=5 and c=13 (vertical white lines) has been analyzed as a function of time. A straight line just ahead of the crack tip is probed for strains and strain rates, at points (white circles with blue outline) labeled  $P_5$  to  $P_{13}$ . Location of this straight line is just below the initial crack plane and corresponds, approximately, to the region of maximum shear strain.  $P_5$  to  $P_{13}$  lie on columns of Cu dots from c=5 to c=13. (Color version online.)

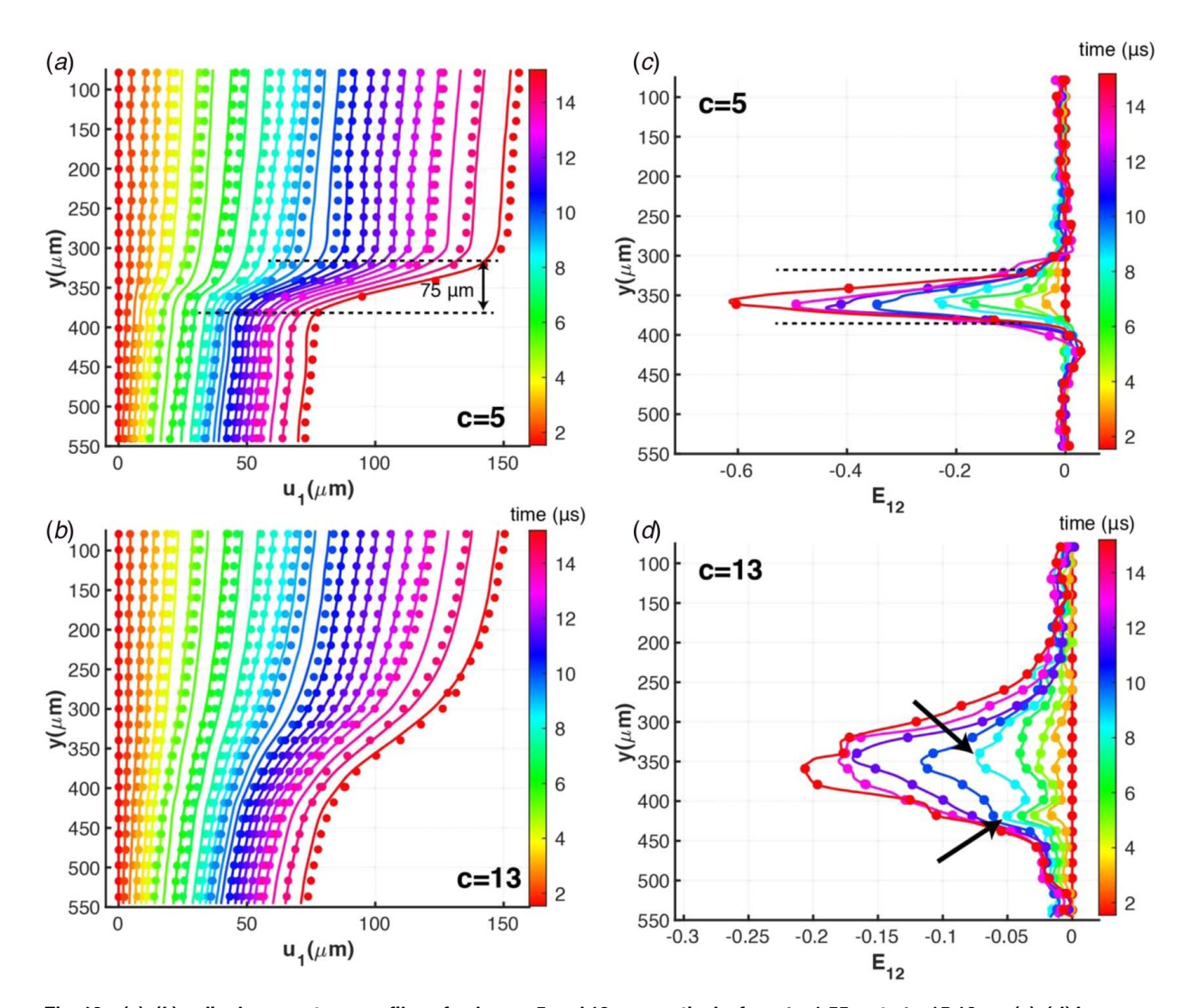


Fig. 13 (a), (b) x-displacement,  $u_1$ , profiles of columns 5 and 13, respectively, from  $t = 1.55 \,\mu$ s to  $t = 15.19 \,\mu$ s. (c), (d) Lagrangian shear strain,  $E_{12}$ , profiles of columns 5 and 13, respectively, from  $t = 1.55 \,\mu$ s to  $t = 15.19 \,\mu$ s. The dots on displacement and shear strain profiles indicate the experimentally measured values at particle centroids. Note that the shear strain profiles are not drawn at all time instants captured, to allow for clarity in the figures. A localized region of plastic deformation is shown for column 5 in (a), (b), (d), and (e) using dotted lines. In (d), shear strain is shown to localize in two bands (black arrows) at earlier times. At later times, the band on the top takes over while the band at the bottom is suppressed.

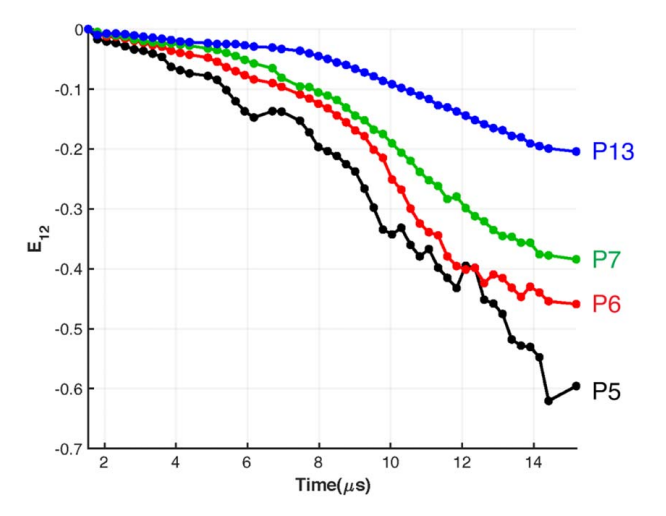


Fig. 14  $E_{12}$  versus time at points  $P_5$ ,  $P_6$ ,  $P_7$ , and  $P_{13}$ . Data closer to the notch tip are noisier as expected. The magnitude of the shear strain rate increases at  $t \approx 8 \,\mu\text{s}$ , as shown by the arrows.

resolution can be achieved by decreasing the dot diameter and the pitch.

Shear strains are plotted at multiple points ahead of the crack tip as shown in Fig. 14. Despite the noise, especially near the notch tip, an increase in the shear strain rate can be seen at  $t \sim 7-8 \mu s$  for all locations. Such a transition in the shear strain rate is a possible kinematic signature of the onset of localization near the crack tip. Shear strain rate magnitude of the order of  $10^5 \text{ s}^{-1}$  can be inferred for  $P_5$ . As expected, points away from the crack tip experience smaller strain rate magnitudes compared with those near the crack tip.

To sum up, the experimental method described above combines high spatial and temporal resolutions. Its application to study crack tip deformation in polycarbonate specimens subjected to predominantly mode II loading allows: (i) direct measurement of the evolution of the kinematic fields near the crack tip subjected to transient loading at micron-scale spatial resolution; (ii) in situ measurement of the width of the strain localization band; (iii) observation of two incipient shear localization bands, one of which eventually becomes the dominant band while the other gets suppressed; and (iv) identification of a possible kinematic signature associated with initiation of the shear band in the form of a distinct increase in the shear strain rate ahead of the crack tip. Note that these include new insights into the formation of SBs in polycarbonate as a result of imaging at high spatial and temporal resolutions simultaneously.

As noted above, the experimental setup described above measures the near crack tip kinematic fields only. Determination of the stress fields and prediction of the observed experimental features would require a reliable thermomechanical constitutive model of polycarbonate over a wide range of strain rates and temperatures. In other words, the experimental observations offer benchmark data to examine the accuracy of constitutive models. In Sec. 5, a computational simulation effort is presented that makes use of a constitutive model for polycarbonate, which is a modified version of a model reported in the recent literature. The simulations are carried out to interrogate the potential spatial and temporal resolution limitations in the experiments. A comparison between the simulation and the experimental results can help guide experimental improvements (and possibly model improvements as well).

# 5 Computational Simulations

**5.1** A Constitutive Model for Polycarbonate. A specialized rate-dependent thermomechanical model that was previously developed and presented in Refs. [44–47] is used in the simulations presented here. Compared with the general amorphous polymer model

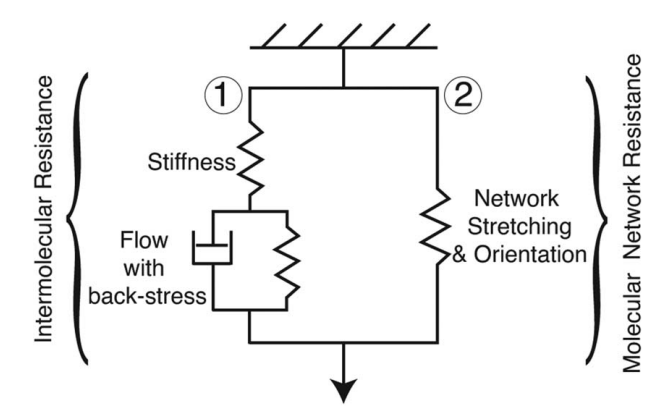


Fig. 15 A schematic of spring-dashpot representation of the model

in Refs. [44–47], here we have chosen different (simplified) relations for some of the temperature and rate-dependent material parameters. These simplified relations reduce number of model parameters that are needed for polycarbonate. For completeness, we summarize the specialized model and material parameters for polycarbonate that were used for simulations. Polycarbonate is assumed to follow a rheological model consisting of two micromechanisms as shown in Fig. 15. The first mechanism is a nonlinear spring-dashpot in which the spring represents an elastic intermolecular bond-stretching, and the dashpot represents thermally activated inelastic flow due to chain-segment rotation and relative slippage of the polymer chains between neighboring mechanical cross-linkage points. The second micromechanism is a nonlinear spring that represents changes in the free energy and corresponding elastic response due to stretching of the molecular chain networks.

The two micromechanisms in Fig. 15 are represented using superscripts (1) and (2). The total free energy density per unit reference volume for the glassy polymer is taken as

$$\psi_R = \psi^{(1)} + \psi^{(p)} + \psi^{(2)} \tag{6}$$

Here,  $\psi^{(1)}$  is a free energy of intermolecular interactions represented by the "stiffness" spring in Fig. 15 and modeled using the elastic Right-Cauchy Green tensor,  $C^e$ ;  $\psi^{(2)}$  is a free energy associated with the stretching of polymer chain network (represented as a spring in the second micromechanism in Fig. 15) and modeled using the total Right-Cauchy Green tensor, C.  $\psi^{(p)}$  ( $\equiv \psi^{(p)^{(1)}}$  for the spring parallel to the dashpot in the first micromechanism) is an energy associated with inelastic deformation and assumed to depend on an internal variable tensor, A. This energy leads to the development of a *back-stress* that allows modeling Bauschinger-like response observed in cyclic loading of polymers. The free energy,  $\psi^{(1)}$  is defined as

$$\psi^{(1)} = G|E^{e}|^{2} + \frac{1}{2}\left(K - \frac{2}{3}G\right)(trE^{e})^{2} - 3K\alpha(\theta - \theta_{0})(trE^{e})$$
$$-\frac{c}{2\theta_{0}}(\theta - \theta_{0})^{2} \tag{7}$$

where  $E^e$  is an elastic logarithmic strain measure and G, K,  $\alpha$ , c,  $\theta_0$  are the shear modulus, bulk modulus, coefficient of thermal expansion, specific heat capacity, and reference temperature, respectively. The free energy component  $\psi^{(2)}$  is taken to account for network stretching using the Gent model [48]:

$$\psi^{(2)} = -\frac{1}{2}\mu_R I_m \ln\left(1 - \frac{I_1 - 3}{I_m}\right) \tag{8}$$

where  $I_1 \stackrel{\text{def}}{=} tr C_{dis}$  is the first principal invariant of the distortional Right-Cauchy Green tensor ( $C_{dis}$ ).  $\mu_R$  and  $I_m$  are two materials parameters, representing the ground-state rubbery shear modulus

and limited chain extensibility, respectively. We have selected the Gent model in our study. Other nonlinear rubber elastic models [49,50] can also be considered to mathematically represent free energy from polymer chain network stretching.

With the tensorial variable A defined in a form similar to a logarithmic strain as

$$\ln A = \sum_{i=1}^{3} \ln a_i \, \boldsymbol{l}_i \otimes \boldsymbol{l}_i \tag{9}$$

where  $l_i$  are the principal directions of **A**, the inelastic free energy  $\psi^{(p)}$  is taken as

$$\psi^{(p)} = \frac{1}{4}B[(\ln a_1)^2 + (\ln a_2)^2 + (\ln a_3)^2]$$
 (10)

where B is a back-stress modulus. The evolution equation for tensorial internal state variable A is taken as

$$\dot{A} = \mathbf{D}^p A + A \mathbf{D}^p - \gamma \nu^p A \ln A, \quad \text{with } A(X, 0) = 1$$
 (11)

where  $\gamma \ge 0$  is a parameter that controls the dynamic recovery of A and  $\nu^p$  is an equivalent plastic shear strain rate. In the evolution Eq. (11) for A, the term  $\gamma \nu^p A \ln A$  represents a dynamic recovery term. In the absence of this dynamic recovery term, A will evolve same as the Cauchy Green inelastic tensor  $B^p$ . Corresponding to the free energy Eq. (6) and the schematic in Fig. 15, the Cauchy stress for glassy polycarbonate is given by

$$T = T^{(1)} + T^{(2)} \tag{12}$$

where each of the terms on the right-hand side correspond to the stress due to the corresponding micromechanism described above. For the free energy  $\psi^{(1)}$  in Eq. (7), the Mandel stress is

$$M^{e} = 2GE_{0}^{e} + K(trE_{0}^{e})1 - 3K\alpha(\theta - \theta_{0})1$$
 (13)

The corresponding contribution to the Cauchy stress from micromechanism 1 (intermolecular resistance) can be obtained as

$$\boldsymbol{T}^{(1)} = J^{-1} \boldsymbol{R}^e \boldsymbol{M}^e \boldsymbol{R}^e T \tag{14}$$

where  $\mathbf{R}^{e}$  is the rotation tensor of elastic deformation gradient  $\mathbf{F}^{e}$ . For the free energy  $\psi^{(2)}$  in Eq. (8), the contribution from network stretching (micromechanism 2) is given as

$$T^{(2)} = J^{-1} \mu_R \left( 1 - \frac{I_1 - 3}{I_{vi}} \right)^{-1} (\mathbf{B}_{dis})_0$$
 (15)

where  $(B_{dis})_0$  is the deviatoric part of the distortional Left-Cauchy Green tensor. For the inelastic free energy,  $\psi^{(p)}$  in Eq. (10), a back-stress (symmetric and deviatoric) is obtained as

$$M_{back} = B \ln A \tag{16}$$

The driving stress for plastic flow is an effective stress given by

$$(\boldsymbol{M}_{eff}^{e})_{0} = \boldsymbol{M}^{e} - \boldsymbol{M}_{back} \tag{17}$$

The equivalent shear stress and mean normal pressure are defined as

$$\bar{\tau} \stackrel{\text{def}}{=} \frac{1}{\sqrt{2}} |(\boldsymbol{M}_{eff}^{e})_{0}|, \quad \text{and } \bar{p} \stackrel{\text{def}}{=} -\frac{1}{3} tr \boldsymbol{M}^{e}$$
 (18)

respectively.

We use the Kroner-Lee multiplicative decomposition of the deformation gradient, F, into elastic ( $F^e$ ) and inelastic ( $F^p$ ) parts as  $F = F^e F^p$ . Kroner-Lee decomposition has been frequently used in literature for a variety of viscoelastic and elasto-plastic modeling

[51,52]. With  $D^p$  as plastic stretching tensor, for the flow rule, the evolution equation for  $F^p$  is assumed as

$$\dot{\boldsymbol{F}}^{p} = \boldsymbol{D}^{p} \boldsymbol{F}^{p}, \quad \boldsymbol{F}^{p}(\boldsymbol{X}, 0) = 1, \quad \boldsymbol{D}^{p} = \nu^{p} \left( \frac{(\boldsymbol{M}_{eff}^{e})_{0}}{2\bar{\tau}} \right),$$

$$\boldsymbol{\tau}^{e} = \bar{\tau} - (S_{1} + S_{2} + \alpha_{p}\bar{p}),$$

$$\boldsymbol{\nu}^{p} = \begin{cases} 0 & \text{if } \tau^{e} \leq 0, \\ \nu_{0} \exp\left(-\frac{Q}{k_{R}\theta}\right) \left[ \sinh\left(\frac{\tau^{e}V}{2k_{R}\theta}\right) \right]^{1/m} & \text{if } \tau^{e} > 0 \end{cases}$$
(19)

where  $\nu^p$  is an equivalent plastic shear strain rate,  $\tau^e$  is a net shear stress for plastic flow;  $\alpha^p$  is a pressure-sensitivity parameter;  $\nu_0$  is a rate parameter; Q is an activation energy;  $k_B$  is Boltzmann's constant; V is an activation volume; and m is a strain rate sensitivity parameter.  $S_1$  and  $S_2$  are internal state variables.  $S_1$  represents transient shear resistance due to microstructural disordering, and  $S_2$  models increasing shear resistance to plastic flow as chains are stretched and interact with each other at large strains.

It is assumed that the material disorders with applied plastic deformation and causes microscale dilatation, which increases the value of  $\varphi$  (a disorder parameter). Increase in disorder affects resistance  $S_1$  and results in a transient change in the flow stress of the material during plastic deformation. The evolution of stress-like resistance  $S_1$  is coupled to disorder parameter  $\varphi$ . Internal variables  $S_1$  and  $\varphi$  are taken to obey the following coupled evolution equations:

$$\dot{S}_1 = h_1(S_1^* - S_1)\nu^p$$
, with  $S_1^* = b(\varphi^* - \varphi)$ , and  $S_1(X, 0) = 0$ 
(20)

and

$$\dot{\varphi} = g(\varphi^* - \varphi)\nu^p, \quad \text{with } \varphi(X, 0) = 0$$
 (21)

where  $\varphi^*$  denotes the critical value for the order parameter such that  $\varphi < \varphi^*$  implies that the material disorders whereas  $\varphi > \varphi^*$  implies that material becomes less disordered. The evolution of  $S_2$  is assumed as

$$\dot{S}_2 = h_2(\bar{\lambda}^p - 1)(S_2^* - S_2)\nu^p, \text{ with } S_2(X, 0) = 0$$
 (22)

where  $h_2$  and  $S_2^*$  are constants,  $\mathbf{B}^p$  as the inelastic Left-Cauchy Green tensor and  $\bar{\lambda}^p \stackrel{\text{def}}{=} \sqrt{tr\mathbf{B}^p/3}$  is the effective plastic stretch. For temperature-dependent parameters in the model, the following relations are used:

$$B(\theta) = X(\theta_{g} - \theta) \tag{23}$$

$$\varphi^*(\theta) = k_1 + k_2(\theta_g - \theta) \tag{24}$$

$$g(\theta) = g_1 + g_2(\theta_g - \theta) \tag{25}$$

$$\mu_R(\theta) = \mu_0 + N(\theta_g - \theta) \tag{26}$$

where  $\theta_g$  is the glass transition temperature of the polymer, and X,  $k_1$ ,  $k_2$ ,  $g_1$ ,  $g_2$ ,  $\mu_0$ , and N are temperature related material parameters. Balance of energy gives the following equation for temperature:

$$c\dot{\theta} = -Div \ \boldsymbol{q}_R + q_R + \omega \left(\bar{\tau} + \frac{1}{2}B\gamma |\ln A|^2\right) \nu^p$$
 (27)

where  $q_R$  is the heat flux in reference frame, c is the specific heat, and  $\omega \approx 0.8$  is the fraction of plastic work converted to heat.

**5.2 Model Parameters for Polycarbonate.** Parameters for polycarbonate were calibrated using simple compression experiments conducted at various strain rates and temperatures below the glass transition temperature,  $\theta_g$  of the polymer [45,47]. The calibrated material parameters are shown in Table 3 (parameter calibration was conducted since the parameters in the modified model used here differ from those the previously published in Refs. [45,47]).

Table 3 Material parameters for PC

Parameter	Value	Parameter	Value
$\theta_g(K)$	418	$h_1$	58
G (MPa)	638	b (MPa)	5850
$\nu_{poi}$	0.37	$g_1$	10.3
X (MPa/K)	1.5	$g_2 (K^{-1})$	-0.038
γ	26	$k_1$	$2.6 \times 10^{-3}$
$\alpha_p$	0.12	$k_2 (K^{-1})$	$1.5 \times 10^{-5}$
$\nu_0^r (s^{-1})$	$2.1 \times 10^{16}$	$h_2$	0.12
m	0.08	$S_2^*$ (MPa)	150
Q(J)	$1.46 \times 10^{-19}$	$\mu_0$ (MPa)	4
$V(m^3)$	$2.95 \times 10^{-28}$	N (MPa/K)	$11.4 \times 10^{-2}$
		$I_m$	7.5

The model fit to the experiments for PC at 25 °C, 70 °C, and 105 °C and at strain rates  $0.001~{\rm s}^{-1},~0.01~{\rm s}^{-1},~and~0.1~{\rm s}^{-1}$  is shown in Fig. 16. The predictions of calibrated model for the room temperature high strain rate experimental stress–strain results from Garg et al. [53] at rates of 0.5 s<sup>-1</sup> and 3400 s<sup>-1</sup> are shown in Fig. 17(a). A comparison of model predicted temperature rise and Garg et al. [53] measurements are shown in Fig. 17(b).

# **6 Numerical Modeling Results**

The constitutive model described above is implemented in ABAQUS through a user sub-routine (VUMAT). The mesh for a specimen region around the notch is shown in Fig. 18. In the region behind the notch, a structured mesh with an element size

of 5  $\mu$ m is used. The sample geometry is meshed with eight-noded thermally coupled three-dimensional brick elements. The simulation geometry also includes the striker and incident bar in the model, which are not shown here. Displacement, strain, stress, and temperature fields are extracted at locations that match with the corresponding points in the experiments.

Simulated  $u_1$  displacements and shear strains ( $E_{12}$ ) in columns close to the notch tip (c=5) and farther away (c=13) are compared with experimental observations in Figs. 19 and 20, respectively. In general, there is a good agreement between the simulated and experimental displacements (Fig. 19). At early times, simulations slightly under-predict the displacement magnitudes but match well with the experimental observations at later times. However, shear strains near the crack tip (Fig. 20(a)) predicted by the simulations are higher in magnitude than those seen in experiments. For column 5, the simulations predict a shear strain localization zone of ~70  $\mu$ m (Fig. 20(a)), which is in close agreement with the experimentally observed value of ~75  $\mu$ m for column 5.

For the region farther away from the notch tip, e.g., for column 13, simulated shear strain localizes into three different bands (Fig. 20(b)) as opposed to a single band observed experimentally. The presence of these bands can be seen in Fig. 19(b) as well in which the undulations introduce deviation between the simulated and measured displacements. The evolution of shear localization in the simulations is better visualized through the strain fields at different times, as shown in Fig. 21. The shear strain is shown to localize in a single band at earlier times (Figs. 21(a) and 21(b)) and then divide into three bands at latter times (Figs. 21(c) and 21(d)). It should be kept in mind that the constitutive model used does not account for damage and fracture of polycarbonate, which would

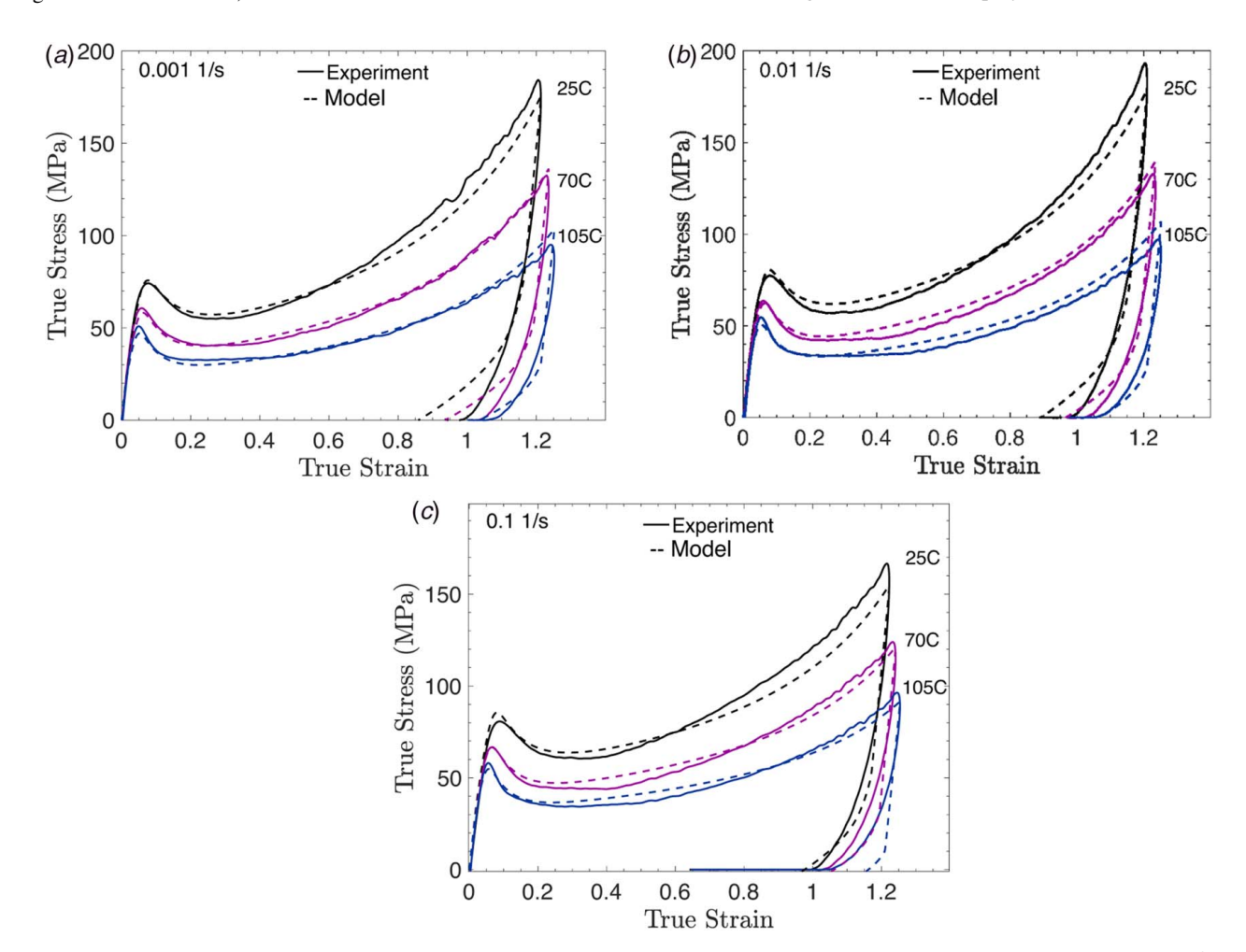


Fig. 16 Fit to the model for experimental stress–strain curves for PC at 25 °C, 70 °C, 105 °C and at strain rates of (a)  $10^{-3}$ , (b)  $10^{-2}$ , and (c)  $10^{-1}$  s<sup>-1</sup>. Experimental data are plotted at solid lines and the model fit is shown as dashed lines.

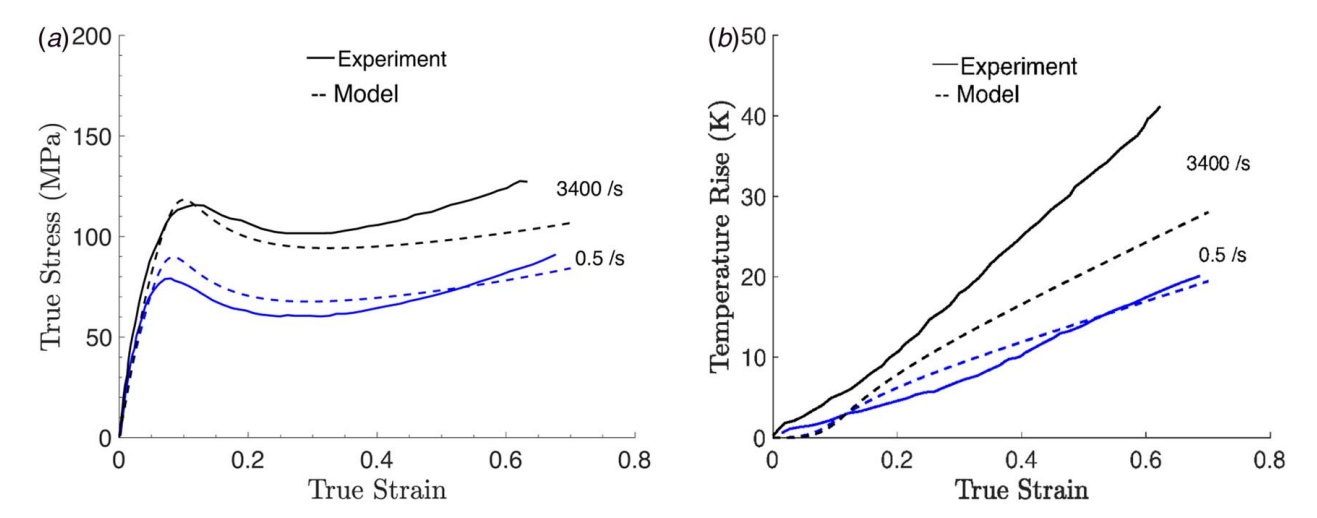


Fig. 17 Comparison of constitutive model predictions against high strain rate compression experiments at  $0.5 \, \mathrm{s}^{-1}$  and  $3400 \, \mathrm{s}^{-1}$ , at an initial temperature of 25 °C. (a) Stress–strain and (b) the corresponding rise in surface temperature of the specimens. The experimental data from Garg et al. [53] are plotted as solid lines while the model predictions are shown as dashed lines.

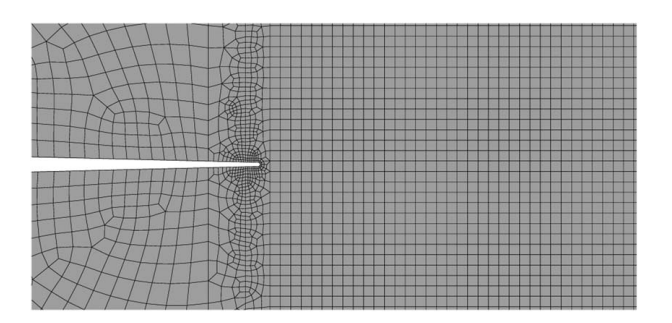


Fig. 18 Mesh for simulations of edge-on impact of polycarbonate plate. Region ahead of the notch uses a structured mesh with an element size of  $5 \mu m$ , whereas the region behind the notch tip has a free mesh with much smaller elements near the notch tip.

lead to an artificial accumulation of shear strains beyond what the material can sustain in reality. If the material damage and consequent loss of strength are accounted for, one of the multiple bands would be expected to grow while suppressing the others. However, the tendency to form multiple bands is in good qualitative agreement with the experimental observation discussed in Sec. 6.2

in the context of Fig. 13(d) in which two incipient localization bands are seen.

Furthermore, shear strain evolution is compared for a few points on the crack plane in Fig. 22. The simulation results are in reasonable qualitative agreement with the experiments, i.e., the simulations predict transition to a higher strain rate when the material localizes. However, significant quantitative differences emerge at later times. There are two features worth noting here. The simulations support the proposition discussed in Sec. 6.2 that the quick transition to a higher strain rate ahead of the crack tip is associated with the localization event. The quantitative differences between the strain rate histories can be attributed to the fact that the constitutive model was calibrated up to strain rates of  $\sim 10^3/\text{s}$  that are orders of magnitude less that what is experienced within the shear band ( $\sim 10^5/\text{s}$ ). The absence of damage in the constitutive model further contributes to the observed differences.

## 7 Discussion and Summary

An experimental method capable of capturing dynamic failure events at high spatial and temporal resolutions simultaneously is reported here. The setup can capture images at rates of up to

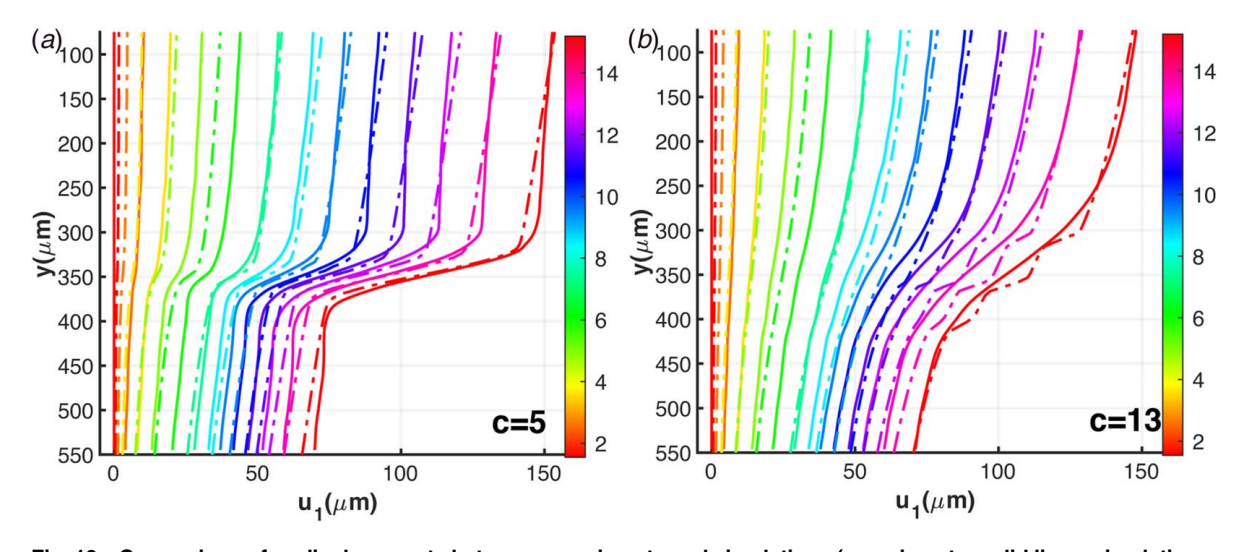


Fig. 19 Comparison of  $u_1$  displacements between experiments and simulations (experiments: solid lines, simulations: dotted lines) for columns 5 and 13

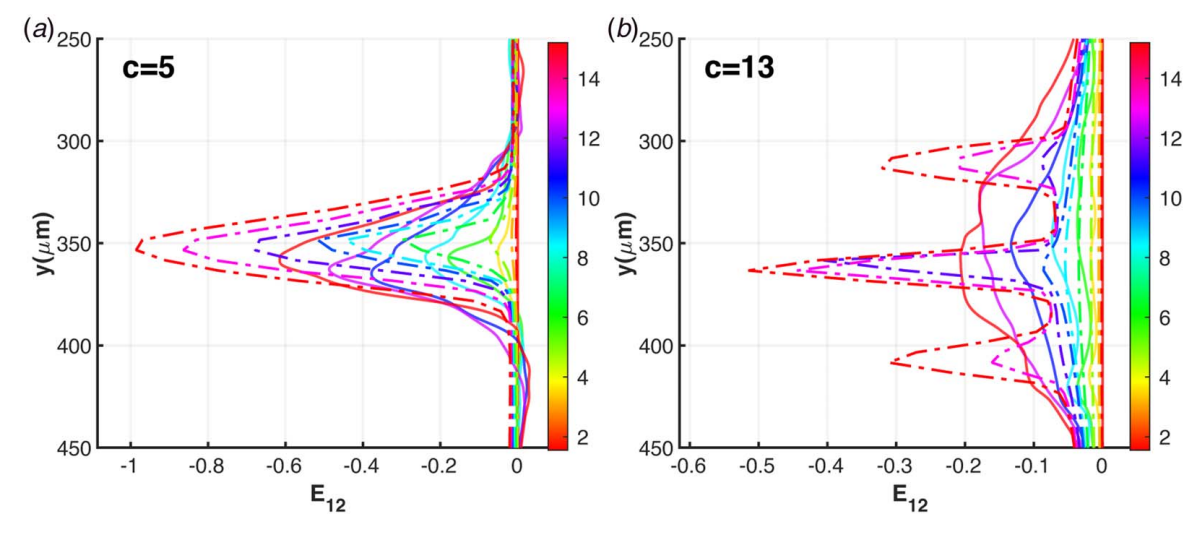


Fig. 20 Comparison of shear strains ( $E_{12}$ ) between experiments and simulations (experiments: solid lines, simulations: dotted lines) for columns 5 and 13. The range of y-axis is shortened compared with Fig. 13 to focus on a smaller region of interest.

4 million fps at a sub-micron spatial resolution by using a commercial high-speed camera, coupled with custom built optics and a high-power pulsed laser. The method is demonstrated by imaging the deformation field near a crack tip subjected to dynamic loading to initiate a shear band. Pre-notched polycarbonate plates are impacted on the edge in a Kolsky-bar while measuring the evolution of the displacement field through a micro-dot pattern deposited on the specimen surface. Displacement and strain fields indicate localization of deformation in a  $\sim$ 75  $\mu$ m wide band near the crack tip. A sharp increase in the shear strain rate appears to be the kinematic signature of the onset of localization. More broadly, it is anticipated the technique reported here can help understand the role of microscale material heterogeneities in the mechanisms of fracture and failure during high strain rate loading of materials and structures.

Previous experimental studies by Zhou et al. [12], Guduru et al. [13], Guduru [30], Bjerke et al. [54], Zehnder et al. [55], Ravi-Chandar et al. [28] and Ravi-Chandar [29] have all measured the

elastic stress field in a large region (of the order of a few centimeters) surrounding the crack tip. In contrast, this study focuses on the near crack tip strain fields within the plastic zone and the subsequent localization. As noted in Sec. 6, an important insight from this study is a direct measurement of the shear bandwidth in polycarbonate ( $\sim 75~\mu m$ ). There have been a number of estimates of the shear bandwidth based on evolution models reported in the literature. For example, Wright [56] presented an expression for half bandwidth in terms of material properties and local loading conditions as follows:

$$\delta_{\rm M} = \sqrt{\left(\frac{2mk}{s\lambda\hat{a}}\right)_c} \tag{28}$$

where  $\delta_M$  is the mechanical half bandwidth, k is the thermal conductivity, s is the shear strength of the material,  $\dot{\gamma}$  is the shear strain rate,

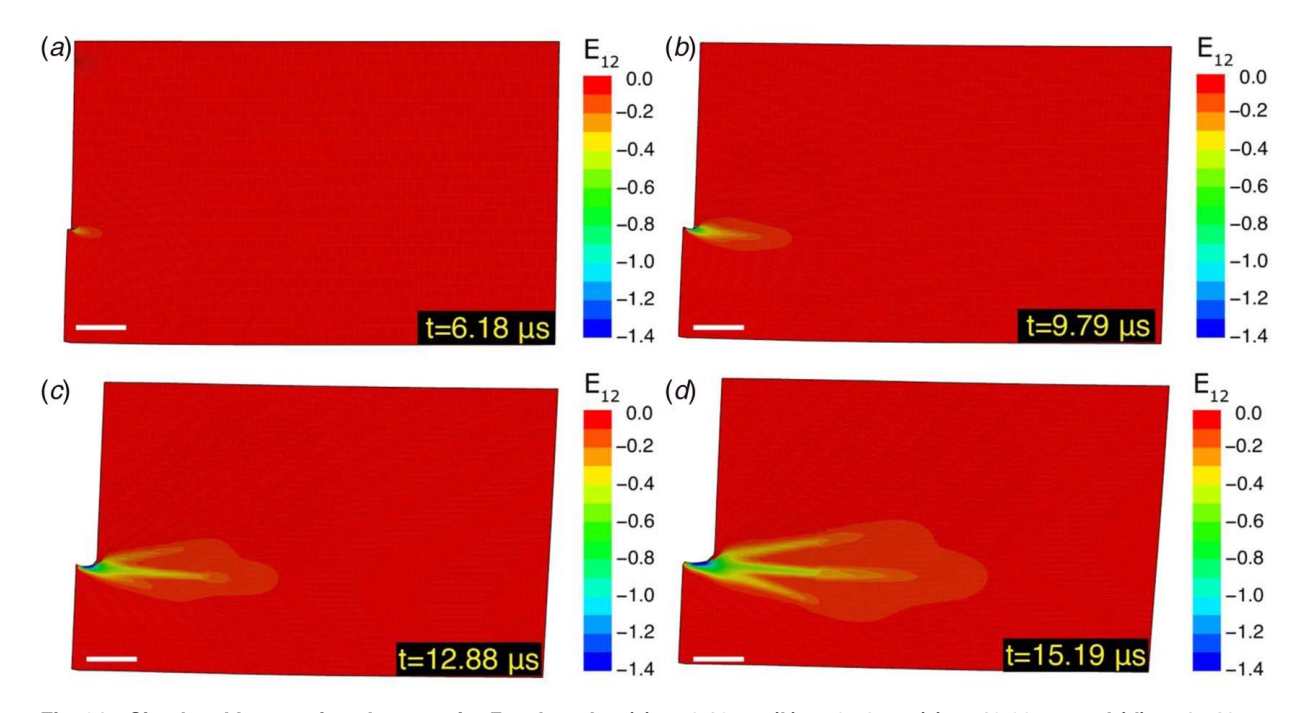


Fig. 21 Simulated Lagrangian shear strain,  $E_{12}$  plotted at (a)  $t = 6.18 \,\mu$ s, (b)  $t = 9.79 \,\mu$ s, (c)  $t = 12.88 \,\mu$ s, and (d)  $t = 15.19 \,\mu$ s. The scale bar (shown in white at the bottom left of each figure) is  $100 \,\mu$ m.

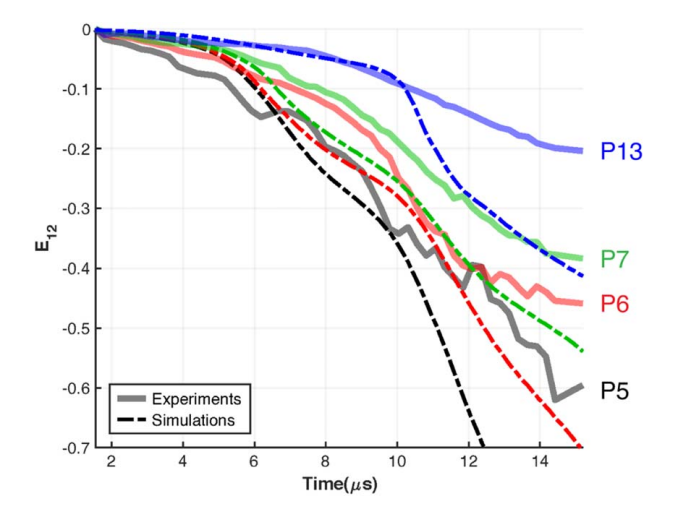


Fig. 22 Comparison of experimental and simulated shear strains at points P5–P13. Experimental shear strains are shown as solid lines while the simulated shear strains are shown as dotted lines.

m is the strain rate sensitivity,  $\hat{a}$  is the relative thermal softening, and  $\lambda$  is a parameter related to shear strain rate through  $\dot{\gamma} = \lambda e^{-z/m_c}$ where  $m_c$  is a small constant and z is a function of temperature. Using the yield strength model for polycarbonate presented by Aranda-Ruiz et al. [57] and taking a shear strain rate of 10<sup>5</sup> s<sup>-1</sup> (obtained in the experiments above), the shear bandwidth predicted from Eq. (31) is in the range 3–5  $\mu$ m. The predicted value is an order of magnitude smaller than the observation ( $\sim$ 75  $\mu$ m). Moreover, as seen in Fig. 20, the simulations also predict a shear bandwidth similar to that in the experiments. However, as noted above, a finer scale band beyond the measurement resolution cannot be ruled out. The discrepancy between the experimental and theoretical (Eq. (31)) shear bandwidths indicates an opportunity to revisit theoretical models of shear band evolution, particularly for polymeric materials such as polycarbonate; or further enhancement in spatial resolution of the experimental technique to resolve finer features.

The main findings of the work can be summarized as follows:

- (i) A high-speed microscopy setup is reported for imaging dynamic events at high spatial (<1 μm) and temporal resolutions (250 ns) simultaneously.
- (ii) The experimental setup is used to image the deformation field near a crack tip subjected to dynamic and predominantly mode II loading. The field of view is approximately 1.07 mm × 0.6 mm. A microfabricated micro-dot pattern on the specimen surface allows deformation and strain field imaging through a particle tracking method. The following insights are enabled through the combination of high spatial and temporal resolutions:
  - (a) The width of the shear band that forms near the crack tip, which is a salient feature of the band that emerges from a combination of the dynamic mechanical and thermal properties of the material, is directly measured to be  $\sim$ 75  $\mu$ m.
  - (b) An estimate of the shear bandwidth based on a classical shear band models in the literature underpredicts the shear bandwidth by an order of magnitude, which offers an opportunity to refine the theoretical models for shear band evolution in polycarbonate and other similar polymers. It also highlights the need for further enhancement in the spatial resolution of the experimental technique to examine the possibility of formation of finer scale features within the currently observable band.
  - (c) The measured shear strain field in the vicinity of the crack tip reveals the presence of two incipient

- localization bands. One of them eventually takes over the localization process while the other is suppressed. This observation motivates the need to develop a theoretical framework to predict and understand the mechanics of initiation and growth of multiple shear bands from a crack tip in polycarbonate and other similar polymers.
- (d) From the experimental measurements, a rapid increase in the shear strain rate at material points ahead of the crack tip appears to be a kinematic signature of the onset of shear localization.
- (iii) A computational simulation of the experiment has been carried out in which an independently calibrated constitutive model of polycarbonate is used. The constitutive model includes two micromechanisms to represent intermolecular and molecular network response. The results of the simulations and their comparison with the experimental observations offer the following insights:
  - (a) The computational simulations reveal the shear bandwidth near the notch tip to be close to that measured in the experiments, which can be viewed as a good benchmark validation of the constitutive model used under extreme loading conditions.
  - (b) The computational simulations can accurately capture the evolution of displacement fields, both near and far from the notch tip. The simulations also support the proposition that the rapid transition to a higher shear strain rate ahead of the notch tip corresponds to the onset of shear localization.
  - (c) Simulations indicate larger shear strain magnitudes than observed experimentally, resulting possibly from a finer mesh size compared with the pitch of dots in experiments. Therefore, there is a need to design future experiments with higher spatial resolution than achieved here.
  - (d) The constitutive model needs better calibration at higher strain rates and needs to account for damage and fracture for more realistic predictions.

## Acknowledgment

The authors gratefully acknowledge funding from the Air Force Office of Scientific Research (Grant No. FA9550-15-1-0415) and the National Science Foundation (Grant No. 1825582).

# **Conflict of Interest**

There are no conflicts of interest.

#### **Data Availability Statement**

The datasets generated and supporting the findings of this article are obtainable from the corresponding author upon reasonable request. The authors attest that all data for this study are included in the paper.

#### References

- Estrada, J. B., Barajas, C., Henann, D. L., Johnsen, E., and Franck, C., 2018, "High Strain-Rate Soft Material Characterization via Inertial Cavitation," J. Mech. Phys. Solids, 112, pp. 291–317.
- [2] Sick, V., 2013, "High Speed Imaging in Fundamental and Applied Combustion Research," Proc. Combust. Inst., 34(2), pp. 3509–3530.
- [3] Aldén, M., Bood, J., Li, Z., and Richter, M., 2011, "Visualization and Understanding of Combustion Processes Using Spatially and Temporally Resolved Laser Diagnostic Techniques," Proc. Combust. Inst., 33(1), pp. 69–97.
- [4] Böhm, B., Heeger, C., Gordon, R. L., and Dreizler, A., 2011, "New Perspectives on Turbulent Combustion: Multi-Parameter High-Speed Planar Laser Diagnostics," Flow, Turbul. Combust., 86(3–4), pp. 313–341.
- [5] Kohse-Höinghaus, K., and Jeffries, J. B., 2002, Applied Combustion Diagnostics, Taylor and Francis, New York.

- [6] Rubino, V., Rosakis, A., and Lapusta, N., 2017, "Understanding Dynamic Friction Through Spontaneously Evolving Laboratory Earthquakes," Nat. Commun., 8(1), p. 15991.
- [7] Gori, M., Rubino, V., Rosakis, A. J., and Lapusta, N., 2018, "Pressure Shock Fronts Formed by Ultra-Fast Shear Cracks in Viscoelastic Materials," Nat. Commun., 9(1), p. 4754.
- [8] Rubino, V., Rosakis, A., and Lapusta, N., 2019, "Full-Field Ultrahigh-Speed Quantification of Dynamic Shear Ruptures Using Digital Image Correlation,' Exp. Mech., **59**(5), pp. 551–582.
- [9] Dodd, B., and Bai, Y., 2012, Adiabatic Shear Localization: Frontiers and Advances, Elsevier, New York.
- [10] Hartley, K., Duffy, J., and Hawley, R., 1987, "Measurement of the Temperature Profile During Shear Band Formation in Steels Deforming at High Strain Rates," Mech. Phys. Solids, 35(3), pp. 283–301.
- [11] Marchand, A., and Duffy, J., 1988, "An Experimental Study of the Formation Process of Adiabatic Shear Bands in a Structural Steel," J. Mech. Phys. Solids, **36**(3), pp. 251–283.
- [12] Zhou, M., Rosakis, A., and Ravichandran, G., 1996, "Dynamically Propagating Shear Bands in Impact-Loaded Prenotched Plates—I. Experimental Investigations of Temperature Signatures and Propagation Speed," J. Mech. Phys. Solids, 44(6), pp. 981–1006.
- [13] Guduru, P., Rosakis, A., and Ravichandran, G., 2001, "Dynamic Shear Bands: An Investigation Using High Speed Optical and Infrared Diagnostics," Mech. Mater., 33(7), pp. 371-402.
- [14] Guduru, P., Ravichandran, G., and Rosakis, A., 2001, "Observations of Transient High Temperature Vortical Microstructures in Solids During Adiabatic Shear Banding," Phys. Rev. E, 64(3), p. 036128.
- [15] Tippur, H., and Rosakis, A., 1991, "Quasi-Static and Dynamic Crack Growth Along Bimaterial Interfaces: A Note on Crack-Tip Field Measurements Using Coherent Gradient Sensing," Exp. Mech., 31(3), pp. 243-251.
- [16] Tippur, H. V., Krishnaswamy, S., and Rosakis, A. J., 1991, "Optical Mapping of Crack Tip Deformations Using the Methods of Transmission and Reflection Coherent Gradient Sensing: A Study of Crack Tip K-Dominance," Int. J. Fract., **52**(2), pp. 91–117.
- [17] Mason, J., Lambros, J., and Rosakis, A., 1992, "The Use of a Coherent Gradient Sensor in Dynamic Mixed-Mode Fracture Mechanics Experiments," J. Mech. Phys. Solids, 40(3), pp. 641–661.
- [18] Kannan, V., Hazeli, K., and Ramesh, K., 2018, "The Mechanics of Dynamic Twinning in Single Crystal Magnesium," J. Mech. Phys. Solids, 120, pp. 154–178.
- [19] Srivastava, V., Parameswaran, V., Shukla, A., and Morgan, D., 2002, Effect of Loading Rate and Geometry Variation on the Dynamic Shear Strength of Adhesive Lap Joints, in Recent Advances in Experimental Mechanics, Springer, New York, pp. 769-780.
- [20] Srivastava, V., Shukla, A., and Parameswaran, V., 2000, "Experimental Evaluation of the Dynamic Shear Strength of Adhesive-Bonded Lap Joints," J. Test. Eval., 28(6), pp. 438–442.
- [21] Council, N. R., 2011, Opportunities in Protection Materials Science and Technology for Future Army Applications, National Academies Press, Washington, DC.
- [22] Ravindran, S., Tessema, A., and Kidane, A., 2016, "Local Deformation and Failure Mechanisms of Polymer Bonded Energetic Materials Subjected to High Strain Rate Loading," J. Dyn. Behav. Mater., 2(1), pp. 146–156.
- [23] Ravindran, S., Tessema, A., and Kidane, A., 2017, "Multiscale Damage Evolution in Polymer Bonded Sugar Under Dynamic Loading," Mech. Mater., 114, pp. 97-106.
- [24] Tiwari, V., Sutton, M., and McNeill, S., 2007, "Assessment of High Speed Imaging Systems for 2D and 3D Deformation Measurements: Methodology Development and Validation," Exp. Mech., 47(4), pp. 561-579.
- [25] Pierron, F., Cheriguene, R., Forquin, P., Moulart, R., Rossi, M., and Sutton, M. A., 2011, "Performances and Limitations of Three Ultra High-Speed Imaging Cameras for Full-Field Deformation Measurements in Applied Mechanics and Materials," Trans. Tech. Publ., 70, pp. 81-86.
- [26] Wright, T., and Perzyna, P., 2003, "Physics and Mathematics of Adiabatic Shear
- Bands," ASME Appl. Mech. Rev., 56(3), pp. B41–B43.
  [27] Kalthoff, J., 1990, "Transition in the Failure Behavior of Dynamically Shear Loaded Cracks," ASME Appl. Mech. Rev., 43(5S), pp. S247-S250.
- [28] Ravi-Chandar, K. K., Lu, J., Yang, B., and Zhu, Z., 2000, "Failure Mode Transitions in Polymers Under High Strain Rate Loading," Int. J. Fract., 101(1-2), pp. 33-72.
- [29] Ravi-Chandar, K., 1995, "On the Failure Mode Transitions in Polycarbonate Under Dynamic Mixed-Mode Loading," Int. J. Solids Struct., 32(6-7), pp. 925-938.
- [30] Guduru, P. R., 2001, An Investigation of Dynamic Failure Events in Steels Using Full Field High-Speed Infrared Thermography and High-Speed Photography, California Institute of Technology, Los Angeles, CA.

- [31] Kirugulige, M. S., Tippur, H. V., and Denney, T. S., 2007, "Measurement of Transient Deformations Using Digital Image Correlation Method and High-Speed Photography: Application to Dynamic Fracture," Appl. Opt., 46(22), pp. 5083-5096.
- [32] Small, A., and Stahlheber, S., 2014, "Fluorophore Localization Algorithms for Super-Resolution Microscopy," Nat. Methods, 11(3), pp. 267-279.
- [33] Abraham, A. V., Ram, S., Chao, J., Ward, E. S., and Ober, R. J., 2009, "Quantitative Study of Single Molecule Location Estimation Techniques," Opt. Express, 17(26), pp. 23352–23373.
- [34] Cheezum, M. K., Walker, W. F., and Guilford, W. H., 2001, "Quantitative Comparison of Algorithms for Tracking Single Fluorescent Particles," Biophys. J., 81(4), pp. 2378-2388.
- [35] Parthasarathy, R., 2012, "Rapid, Accurate Particle Tracking by Calculation of Radial Symmetry Centers," Nat. Methods, 9(7), pp. 724–726.
- [36] Liu, S.-L., Li, J., Zhang, Z. L., Wang, Z. G., Tian, Z. Q., Wang, G. P., and Pang, D. W., 2013, "Fast and High-Accuracy Localization for Three-Dimensional Single-Particle Tracking," Sci. Rep., 3(1), p. 2462.
- Baek, S., and Lee, S., 1996, "A New Two-Frame Particle Tracking Algorithm Using Match Probability," Exp. Fluids, 22(1), pp. 23-32.
- [38] Pereira, F., Stüer, H., Graff, E. C., and Gharib, M., 2006, "Two-Frame 3D Particle Tracking," Meas. Sci. Technol., 17(7), p. 1680.
- [39] Ohmi, K., and Li, H.-Y., 2000, "Particle-Tracking Velocimetry With New Algorithms," Meas. Sci. Technol., 11(6), pp. 603-616.
- [40] Feng, X., Hall, X., Wu, M. S., and Hui, M., and Y, C., 2014, "An Adaptive Algorithm for Tracking 3D Bead Displacements: Application in Biological Experiments," Meas. Sci. Technol., 25(5), p. 055701.
- [41] Patel, M., Leggett, S. E., Landauer, A. K., Wong, I. Y., and Franck, C., 2018, "Rapid, Topology-Based Particle Tracking for High-Resolution Measurements of Large Complex 3D Motion Fields," Sci. Rep., 8(1), p. 5581.
- [42] Immerkaer, J., 1996, "Fast Noise Variance Estimation," Comput. Vis. Image Underst., 64(2), pp. 300-302.
- [43] Buades, A., Coll, B., and Morel, J.-M., 2005, "A Non-Local Algorithm for Image Denoising," 2005 IEEE Computer Society Conference on Computer Vision and Pattern Recognition (CVPR'05), San Diego, CA, June 20, IEEE, pp. 60-65.
- [44] Srivastava, V., Chester, S. A., and Anand, L., 2010, "Thermally Actuated Shape-Memory Polymers: Experiments, Theory, and Numerical Simulations," J. Mech. Phys. Solids, 58(8), pp. 1100–1124.
- [45] Srivastava, V. S. A., Ames, N. M., and Anand, L., 2010, "A Thermo-Mechanically-Coupled Large-Deformation Theory for Amorphous Polymers in a Temperature Range Which Spans Their Glass Transition," Int. J. Plast., 26(8), pp. 1138-1182.
- [46] Anand, L., Ames, N. M., Srivastava, V., and Chester, S. A., 2009, "A Thermo-Mechanically Coupled Theory for Large Deformations of Amorphous Polymers. Part I: Formulation," Int. J. Plast., 25(8), pp. 1474-1494.
- [47] Ames, N. M., Srivastava, V., Chester, S. A., and Anand, L., 2009, "A Thermo-Mechanically Coupled Theory for Large Deformations of Amorphous Polymers. Part II: Applications," Int. J. Plast., 25(8), pp. 1495-1539.
- [48] Gent, A. N., 1996, "A new Constitutive Relation for Rubber," Rubber Chem. Technol., **69**(1), pp. 59–61.
- [49] Bai, Y., Kaiser, N. J., Coulombe, K. L., and Srivastava, V., 2021, "A Continuum Model and Simulations for Large Deformation of Anisotropic Fiber-Matrix Composites for Cardiac Tissue Engineering," J. Mech. Behav. Biomed. Mater., 121, p. 104627.
- [50] Carroll, M. M., 2019, "Molecular Chain Networks and Strain Energy Functions in Rubber Elasticity," Philos. Trans. R. Soc., A, 377(2144), p. 20180067.
- [51] Lee, E. H., 1969, "Elastic-Plastic Deformation at Finite Strains." J. Appl. Mech., **36**(1), pp. 1–6.
- [52] Kothari, M., Niu, S., and Srivastava, V., 2019, "A Thermo-Mechanically Coupled Finite Strain Model for Phase-Transitioning Austenitic Steels in Ambient to Cryogenic Temperature Range," J. Mech. Phys. Solids, 133, p. 103729.
- [53] Garg, M., Mulliken, A., and Boyce, M., 2008, "Temperature Rise in Polymeric Materials During High Rate Deformation," ASME J. Appl. Mech., 75(1), p. 011009.
- [54] Bjerke, T., Li, Z., and Lambros, J., 2002, "Role of Plasticity in Heat Generation During High Rate Deformation and Fracture of Polycarbonate," Int. J. Plast. 18(4), pp. 549-567.
- [55] Zehnder, A. T., Guduru, P. R., Rosakis, A. J., and Ravichandran, G., 2000, 'Million Frames per Second Infrared Imaging System," Rev. Sci. Instrum., 71(10), pp. 3762-3768.
- [56] Wright, T. W., 2002, The Physics and Mathematics of Adiabatic Shear Bands, Cambridge University Press.
- [57] Aranda-Ruiz, J., Ravi-Chandar, K., and Loya, J., 2020, "On the Double Transition in the Failure Mode of Polycarbonate," Mech. Mater., 140, p. 103242.